This paper should be cited as: Liu, X., Zhao, C., Zhang, Q., Yin, Y., Lu, Z., Samsonov, S., Yang, C., Wang, M. & Tomás, R. 2021. Three-dimensional and long-term landslide displacement estimation by fusing C- and L-band SAR observations: A case study in Gongjue County, Tibet, China. Remote Sensing of Environment, **267**, 112745, doi: https://doi.org/10.1016/j.rse.2021.112745.

Three-dimensional and long-term landslide displacement estimation by fusing C- and L-band SAR observations: A case study in Gongjue County, Tibet, China

Xiaojie Liu [a, b], Chaoying Zhao [a, c, d *], Qin Zhang [a, c, d], Yueping Yin [e], Zhong Lu [f], Sergey Samsonov [g], Chengsheng Yang [a], Meng Wang [h], Roberto Tomás [b]

[a] School of Geological Engineering and Geomatics, Chang'an University, Xi'an 710054, China

[b] Department of Civil Engineering, University of Alicante, Alicante 03080, Spain

[c] Key Laboratory of Western China's Mineral Resources and Geological Engineering, Ministry of Education, Xi'an 710054, China

[d] State Key Laboratory of Geo-Information Engineering, Xi'an 710054, China

[e] China Institute of Geo-environment Monitoring, Beijing 10081, China

[f] Roy M. Huffington Department of Earth Sciences, Southern Methodist University, Dallas, TX 75275, USA

[g] Natural Resources Canada, 560 Rochester Street, Ottawa, ON K1A0E4, Canada

[h] Sichuan Geological Survey, Chengdu 610081, China

* Correspondence: cyzhao@chd.edu.cn; Tel.: +86-29-8233-9251

Abstract

Recently, a large number of synthetic aperture radar (SAR) images has been introduced into landslide investigations with the growing launch of new SAR satellites, such as ALOS/PALSAR-2 and Sentinel-1. Therefore, it is appropriate to develop new approaches to retrieve three-dimensional (3D) displacements and long-term (> 10 years) displacement time series to investigate the spatio-temporal evolution and creep behavior of landslides. In this study, a new approach for the estimation of 3D and long-term displacement time series of landslides, based on the fusion of C- and L-band SAR observations, is presented. This method is applied to map 3D and long-term displacements (nearly 12 years) of the landslides in Gongjue County, Tibet in China; four sets of SAR images from different platforms (i.e., L-band ascending ALOS/PALSAR-1, C-band descending

ENVISAT, and C-band ascending and descending Sentinel-1 SAR datasets) covering the period of January 2007 to November 2018 were collected and exploited. First, the assumption that the landslide moves parallel to its ground surface is used to produce 3D displacement rates and time series by fusing ascending and descending Sentinel-1 SAR images, from which the optimal sliding direction for each pixel of the slope is well estimated. Then, the long-term displacement time-series of the landslide between January 2007 and October 2018 in the estimated sliding direction is recovered by fusing L-band ALOS/PALSAR-1 and C-band Sentinel-1 SAR images. In order to fill the time gap of nearly four years between ALOS/PALSAR-1 and Sentinel-1 SAR images, the Tikhonov regularization (TR) method is developed to establish the observational equation. Moreover, to solve the problem arising from ALOS/PALSAR-1 and Sentinel-1 images with different wavelengths, incidence angles and flight directions, the measurements from ALOS/PALSAR-1 and Sentinel-1 images are both projected to the estimated optimal sliding direction to achieve a unified displacement datum. Our results from ascending and descending Sentinel-1 images suggest that the maximum displacement rates of the study area in the vertical and east-west directions from December 2016 to October 2018 were greater than 70 and 80 mm/year, respectively, and 2D displacement results reveal that the displacement patterns and movement characteristics of all the detected landslides are not identical in the study area. Specifically, the 3D displacement results successfully revealed the spatiotemporal displacement patterns and movement direction of each block of the Shadong landslide, and long-term displacement time series showed for the first time that the maximum cumulative displacement exceeds 1.3 m from January 2007 to October 2018. Moreover, the kinematic evolution and possible driving factors of landslides were investigated using 2D and 3D and long-term displacement results, coupled with hydrological factors and unidimensional constitutive models of the rocks.

Keywords: Landslide; Jinsha River; Tibet; InSAR; 3D displacements; Long-term displacement time series

1 Introduction

Landslides are a major natural geological hazard in many areas of the world. During the last few decades, significant economic losses and fatalities have been caused by landslide hazards worldwide (Froude and Petley, 2018; Lin et al., 2018). More recently, the frequencies and magnitudes of landslide occurrences have increased greatly owing to the influence of global extreme climate and intensive anthropogenic activities (Piciullo et al., 2018). The detection and monitoring of unstable slopes play a crucial role in the management and early warning of geohazards (Dai et al., 2020). Interferometric synthetic aperture radar (InSAR) enables the measurement of surface displacement over wide areas, with precisions of centimeter to sub-centimeter scales. This has been widely used to determine the location of landslides over large areas and to monitor the temporal activities of landslides in specific regions (Dong et al., 2018; Herrera et al., 2013; Hu et al., 2020; Shi et al., 2019). In particular, InSAR-derived displacement information can be used to investigate the mechanisms of landslides, including landslide types (Burrows et al., 2019), triggering factors (Chen et al., 2020), failure modes (Eriksen et al., 2017; Kang et al., 2017), depth and volume estimation, and risk assessment (Hu et al., 2016, 2018; Intrieri et al., 2020).

However, most related studies (Hu et al., 2016; Shi et al., 2020; Wasowski et al., 2020) have characterized such landslide displacements only in the one-dimensional line-of-sight (LOS) direction, owing to the limitations of the SAR imaging geometry and single SAR platform. As a consequence, several challenges have arisen for detailed landslide investigations for the following reasons: (1) it is impossible to map landslide movement orthogonal to the LOS direction (Eriksen et al., 2017), thus causing the omissions of that direction for landslide detection; (2) it is difficult to analyze the dynamics and mechanisms of landslide displacement in complex situations (Samsonov et al., 2020); (3) it is inaccurate to map the boundary of landslides and to invert the depth and volume of unstable slopes. In contrast, spatio-temporal three-dimensional (3D) displacements can provide insights on the landslide mechanisms, which can particularly benefit landslide forecasting and risk management (Hu et al., 2018, 2019). To date, different strategies have been explored to retrieve 3D surface displacements from InSAR observations (Wright et al., 2004; Raucoules et al., 2013; Hu et al., 2014a; Wang and Jonsson, 2015); these strategies are typically used to measure large-gradient displacement caused by geomorphological processes such as glacier movement (Hu et al., 2014b), fast-moving landslides (Li et al., 2019; Raucoules et al., 2013; Shi et al., 2018), volcanic activity (Jo et al., 2017; Schaefer et al., 2019), and earthquakes (He et al., 2019). However, there are few studies on the 3D displacement estimation of slow-moving landslides (Sun et al., 2016; Eriksen et al., 2017; Ao et al., 2019), particularly for 3D time-series displacement estimation.

In general, landslides experience three stages from initiation to failure, including primary creep, steady-state creep, and accelerating creep (Aydan et al., 2014; Intrieri et al., 2019); the entire process can last from months to several decades. It is of great significance to investigate the kinematic evolution and creep behavior of landslides to assess the long-term stability of slope and forecast the time of its failure (Aydan et al., 2014). Therefore, it is necessary to recover the long-term (i.e., longer than 10 years) displacement time series of some known specific landslides. However, different SAR satellites operate at different periods with distinctive imaging geometries (i.e., incidence angle and flight direction) and wavelengths. Thus, it is necessary to develop a new InSAR approach to retrieve long-term displacement time series of landslides by fusing multi-platform SAR observations. To this end, there are two challenging issues that need to be addressed: the first is to link SAR acquisitions from different platforms without overlap in the time domain, and the second is to determine the optimal movement direction of the landslide to which the LOS measurements from different SAR platforms can be transformed. Several researchers have explored the first issue in terms of vertical land subsidence monitoring; for example, Pepe et al. (2016a) used a time-dependent geotechnical model to obtain preliminary information to realize the combination of ENVISAT and COSMO-SkyMed SAR images. However, the displacement of landslides is much more complicated than the vertically dominated land subsidence; thus, there are no previously published studies in which the time-gapped InSAR displacement time series from different SAR platforms are linked in a common direction (e.g., sliding direction of slope). For the second issue, the ideal solution is to define the unique and physical sounding movement direction of the slope. The mean slope angle and aspect derived from digital elevation models (DEMs) was regarded as the overall sliding direction of a landslide in previous studies (e.g., Kang et al., 2017), without considering the sliding direction for each block or pixel of the landslide. Moreover, geologists have demonstrated that the sliding direction of the landslide varies along with displacement evolution (Lu, 2015).

The main objective of this study was to propose a new InSAR-based approach to investigate landslide characteristics, with threefold research outcomes, producing: (1) 3D and long-term time series displacement monitoring, (2) interpretation of kinematic evolution and displacement characteristics, and (3) determination of the creep behaviours and possible driving factors of landslides. The proposed method was used to characterize the landslides over Gongjue County, Tibet, China, using C- and L-band SAR images from three different platforms (i.e., C-band ENVISAT, L-band ALOS/PALSAR-1, and C-band Sentinel-1) that were acquired from January 2007 to November 2018. The study area is situated on the southeast edge of the Qinghai-Tibet Plateau, where a series of large-scale ancient landslides are placed as a result of the coupling effects of the complex geological settings, high annual precipitation, and river erosion (Lu et al., 2019; Li et al., 2021). First, active landslides were detected and mapped using the ALOS/PALSAR-1, ENVISAT, and Sentinel-1 SAR images. Second, the 2D displacement rates and time series of all detected landslides were estimated by the fusion of ascending and descending Sentinel-1 SAR images. Then, 3D displacement rates and time series were calculated for one translational landslide, i.e., the Shadong landslide. Evidence from field geological exploration (Li et al., 2021) illustrated that the Shadong landslide is a giant ancient landslide with characteristic of translational movement. Next, the long-term (nearly 12 years) displacement time series of the Shadong landslide in the sliding direction was retrieved by fusing all three SAR datasets. Finally, the displacement characteristics, kinematic evolution, creep behaviors and possible driving factors of the landslides were analyzed and determined.

2 Study area and datasets

2.1 Study area

The study area is situated on the right bank of the Jinsha River, Gongjue County, Tibet, China (Fig. 1), and has an area of approximately 176 km^2. It belongs to the southeast edge of the Qinghai-Tibet Plateau, with steep topography and complex geological conditions as a result of the rapid uplift of the Qinghai-Tibet Plateau (Wang et al., 2000; Li et al., 2006). The elevation in most parts of the study area is higher than 3000 m a.s.l. reaching more than 4000 m a.s.l. in some regions (Fig. 1). Valleys feature strong “V”-shaped topography due to violent river downward cutting and the rapid uplifting of the Qinghai-Tibet Plateau. The height differences range from 500 to 2000 m, resulting in slope angles of greater than 25° in most slopes. The climate belongs to the continental plateau monsoon, and rainfall is concentrated in the summer each year. The annual average temperature and precipitation are approximately 6.5 °C and 480 mm, respectively. Strong physical weathering on the surface of slope materials has occurred owing to the influence of the climate.

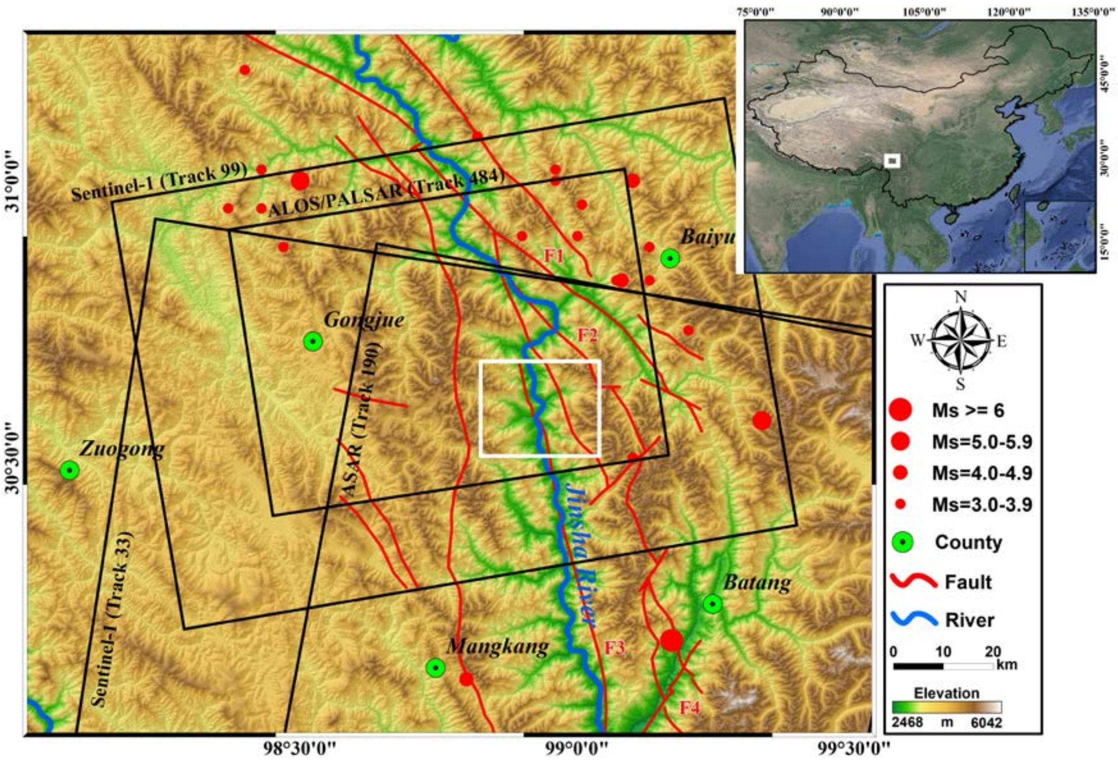

Fig. 1. Location of the study area and coverage of the synthetic aperture radar (SAR) images, with SRTM DEM as the base map. The white and black rectangles represent the study area and the coverage of the SAR images, respectively, and the red dots are the earthquakes that occurred in the study area and vicinity during the period of 1954 to 2019. The red lines are the faults modified from Li et al., 2021, where F1: Jinsha River East Fault; F2: Jinsha River Main Fault; F3: Xiongsong-Suwalong Fault; and F4: Batang Fault.

The geological map with the scale of 1: 250000 in the study area is presented in Fig. 2(a). The outcrops are composed of Paleo-Mesoproterozoic, Lower Triassic, Carboniferous–Permian, Silurian, and Late Triassic strata (Fig. 2). They mainly include plagiogneiss ($Pt_{1-2}Nd$), mica quartz schist (Pt_1g), basalt (Pt_1x), limestone (CPca), carbonate (Sca), quartz diorite (δoT_3), monzonitic granite ($\eta\gamma T_3$), quartz monzonite (ηoT_3), and ultrabasic rocks ($\sum$). The attitude and dip angle of schistosity in the study area greatly vary as the influence of tectonic movements, mainly ranging from 17 to 50°. The tectonic setting is conditioned by a series of NW-trend faults (Li et al., 2021); significant among them are the Jinsha River (F1, F2 and F3 marked in Fig. 1) and Batang faults (F4 marked in Fig. 1) (Chen et al., 2013), thus resulting in frequent seismic activities. There have been approximately 22 earthquakes of $Mw \geq 3.0$ in the study area and its surroundings since 1954, including three stronger earthquakes greater than $Mw = 5.0$, which occurred in 1954, 1979, and 1989.

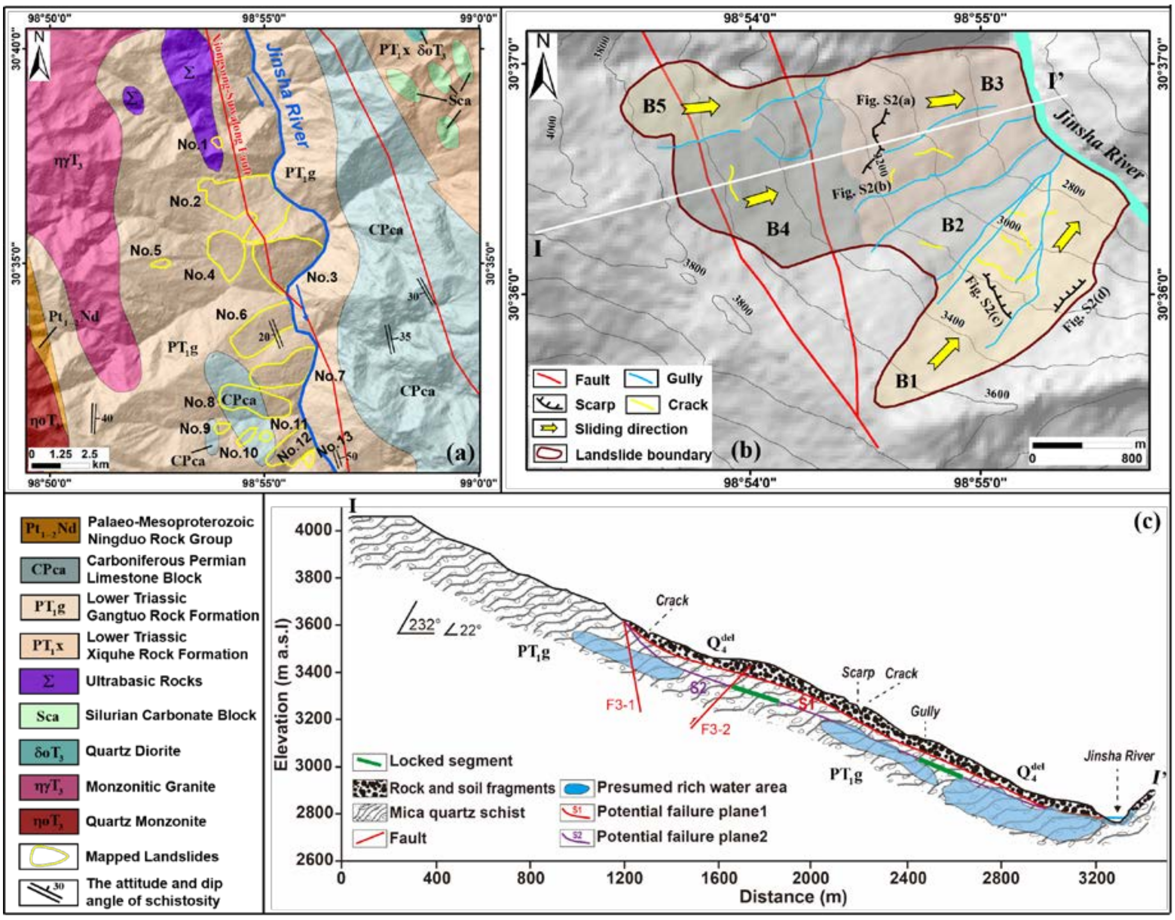

Fig. 2. (a) Geological setting of the study area, with the scale of 1: 250000. The name of the labeled landslides (i.e., No.1 ~ No.13) is listed in Table 2, and the red lines indicate the faults. (b) Shaded relief map of the Shadong landslide, labeled as No.2 in (a). The polygons with different colors represent five blocks (B1-B5) of the landslide. (c) Geological cross section along the Profile I-I' marked in (b), adapted from Li et al., 2021.

The complex geological settings, tectonic movements, high annual precipitation, and river erosion and human activities work together to lead to the extensive distribution and strong activity of large-scale landslides in the study area (Ma et al., 2004; Li et al., 2021). The lithology of the stratum provides favorable geological conditions for the occurrence of landslides, and it is an inherent factor in the formation of landslides. We can see from Fig. 2(a) that the landslides are basically distributed in the Gangtuo Rock Formation (PT_1g) of Lower Triassic. This kind of formation belongs to the weaker rock mass and is prone to slide under the action of shear stress (Li et al., 2021). Generally, rock masses are more likely to fracture in active tectonic zones, and landslide susceptibility directly correlates with the distribution and activity of faults (Guo et al., 2015). It should be mentioned that the Xiongsong-Suwalong fault passes through the Shadong and Sela landslides (No.2 and No.3 labeled in Fig. 2(a)). Heavy rainfall in the summer can lead to the decrease of shear strength of the soil due to the rise of the river water level and water infiltration favoured by the existence of cracks, thus driving the landslide movements. Remote sensing images show that the foot of most of the landslides intersects the Jinsha River. The stress of the foot of the slopes can be changed by the intense scouring and erosion of the Jinsha River; additionally, the variations in the Jinsha River water level can alter the shear strength of slope material, thus generating large-scale pull-type landslides (Lacroix et al., 2020; Li et al., 2021). Landslide hazards greatly endanger the safety of the cities and towns as well as the traffic lines in this area. The landslides could block the Jinsha River when the rupture occurs, thereby also threatening the normal operation of hydropower stations. Previous studies have mapped the distribution of landslides in this area using InSAR and optical remote sensing methods (Lu et al., 2019). However, complete investigations of the landslides in terms of 3D displacements, kinematic evolution, and creep behaviours are absent.

Among the distributed landslides, field survey (Li et al., 2021) and optical image from unmanned aerial vehicle (UAV) measurement (Fig. S1(a)) show that the Shadong landslide (Fig. 2(b)) is a giant ancient landslide, with an area of approximately 5.33 km^2. From the optical image and shaded relief map shown in Figs. S1 (c) and (d), the severe collapse can be evidently seen at the front edge of the landslide, as a result of the erosion of the Jinsha River. Additionally, field geological survey showed that several large scarps and cracks have been developed on the slope surface (Figs. 2(b) and S2), the height of the scarps ranges from 0.5 to 3.0 m, and the width of the cracks ranges from 5 to 150 cm (Li et al., 2021). Based on the geomorphological analysis (Fig. S1(b)), in conjunction with the developments of the gullies, the entire landslide can be divided into five different blocks as shown in different colors in Fig. 2(b). Geomorphic features and slope aspect derived from UAV DEM indicate that these blocks have different sliding directions (Figs. S1 and 2(a)), among which blocks B1, B2 and B4 are moving toward the northeast direction, and blocks B3 and B5 are moving toward the east direction. Moreover, two secondary sliding regions R1 and R2 (Figs. S1(a) and (b)) were found in blocks B1 and B3 respectively, by visual interpretation of UAV image. From the optical image and shaded relief map shown in Figs. S1(e) and (f), we can clearly see that there have been developed two large cracks (yellow arrows in Figs.

S1(e) and (f)) and a scarp (red arrows in Figs. S1(e) and (f)) at the both sides and head of the Region R1, respectively. The landslide is mainly composed of rock and soil fragments (Q_4^{del}) and mica quartz schist (PT_1g) (Fig. 2(c)). The attitude of the bedrock is 190 ~ 256° ∠17 ~ 37° (Li et al., 2021). The Xiongsong-Suwalong fault, a branch of the Jinsha River fault zone, passes through the middle and back sections of the landslide in the NNW direction (Figs. 2(b) and (c)). Field geological exploration revealed that the landslide is a translational slide according to Cruden and Varnes (1996) classification, with two potential failure planes (Li et al., 2021), i.e., S1 and S2 marked in Fig. 2(c). The first failure plane (S1) with a depth of 51 ~ 56 m, corresponds to a landslide volume of 2.67×10^8 ~ 2.88×10^8 m^3; and the second failure plane (S2) with a depth of 101 ~ 115 m, corresponds to a landslide volume of 5.28×10^8 ~ 6.02×10^8 m^3. In addition, field geological exploration found that there are two major locked segments in the middle of the Shadong landslide that control the deep-seated stability of the landslide (Li et al., 2021), as shown by the green lines in Fig. 2(c).

2.2 Datasets

To demonstrate the proposed approach and investigate the detailed landslide characteristics, 165 SAR images composed of four independent SAR datasets from three different sensors onboard the ENVISAT, ALOS/PALSAR-1, and Sentinel-1 satellites were obtained. The spatial coverage of the SAR datasets used in this study is shown in Fig. 1, and the basic parameters of the SAR images are summarized in Table 1. The 2D and 3D displacement rates and time series were estimated using ascending and descending Sentinel-1 SAR images. As there exists a time gap of nearly four years where no SAR images were archived, we recovered the long-term displacement time series in the sliding direction by fusing the ascending ALOS/PALSAR-1 and Sentinel-1 SAR measurements using the Tikhonov regularization method (Tikhonov 1963). It is worth noting that the ALOS/PALSAR-1 images were acquired under both modes of fine-beam dual-polarization (FBD) and beam single-polarization (FBS), and the SAR images in FBD mode were oversampled to the FBS mode in this study to improve the spatial resolution.

Table 1. Basic parameters of SAR images used in this study

Sensors	Track	Orbit	Heading (°)	Incidence angle (°)	Start date dd/mm/yyyy	End date dd/mm/yyyy	No. of images	No. of interferograms
ALOS/PALSAR-1	484	Ascending	-10.29	38.73	02/01/2007	28/02/2011	16	37

ENVISAT ASAR	190	Descending	-168.17	23.54	21/02/2007	13/10/2010	17	35
Sentinel-1	99	Ascending	-10.46	33.85	12/10/2014	03/10/2018	79	198
Sentinel-1	33	Descending	170.02	43.94	01/12/2016	03/11/2018	53	120

We employed a standard differential InSAR (DInSAR) procedure to handle all SAR images as follows. To avoid the influences of temporal and spatial decorrelation, all possible interferometric pairs of the Sentinel-1 dataset were generated using a small baseline subset (SBAS) strategy (Berardino et al., 2002). The spatial and temporal baseline thresholds were set at 250 m and 60 d, respectively. A full combination was conducted to generate the interferograms for the ALOS/PALSAR-1 and ENVISAT datasets, as we had collected a relatively small quantity of SAR data. After the interferogram filtering (Goldstein and Werner, 1998) and phase unwrapping (Costantini, 1998), we carefully checked and processed the errors related to residual topography, phase unwrapping and atmospheric artifacts. Furthermore, the corrected unwrapped interferograms with high quality were finally chosen for further processing. The spatiotemporal baseline combinations of the selected interferograms for each SAR sensor are shown in Fig. 3. To unify the spatial resolution and to map small-scale landslides, the interferograms were multi-looked using factors of 2×5 (range × azimuth) for ALOS/PALSAR-1 images, 1×5 (range × azimuth) for ENVISAT images, and 4×1 (range × azimuth) for Sentinel-1 images. The pixel spacing of the multi-looked images in both the ground-range and azimuth directions was approximately 15 m for the ALOS/PALSAR-1 images, 20 m for the ENVISAT images, and 15 m for the Sentinel-1 images. One arc-second SRTM DEM with a spatial resolution of 30 m was adopted to remove the topographic phase during differential InSAR processing.

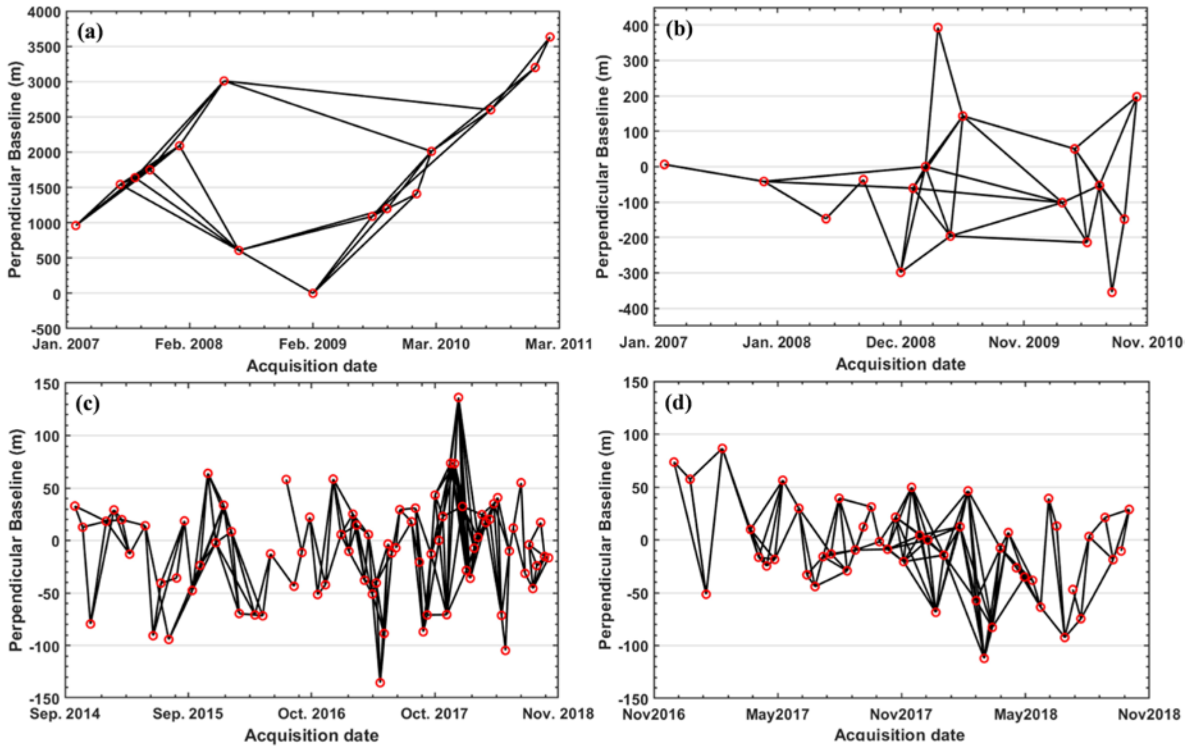

Fig. 3. Spatial-temporal baseline combinations of all interferograms used in this study. (a) ALOS/PALSAR-1 dataset for Path 484; (b) ENVISAT dataset for Path 190; (c) ascending Sentinel-1 dataset for Path 99; and (d) descending Sentinel-1 dataset for Path 33.

3 Methodology

A new approach to fuse C- and L-band SAR images for 3D and long-term displacement time series monitoring of landslides is presented in this section. Figure 4 shows the workflow and main modules of the approach, which can be organized into four steps as follows.

Step 1: Each SAR dataset was processed independently to generate unwrapped interferograms using the standard DInSAR procedure, including interferogram generation; filtering; phase unwrapping; quality checking; and corrections for atmospheric artifacts, DEM errors, and phase unwrapping errors. The high-quality unwrapped interferograms of each SAR dataset were geocoded and resampled to an identical spatial grid in the World Geodetic System 1984 (WGS 84) coordinate system with a spatial resolution of 15 m for further processing. Then, the displacement rate of each SAR dataset in the LOS direction was calculated using the stacking interferograms method (Lyons et al., 2003) to detect and map active landslides. This was done because the combination of multi-platform SAR datasets to detect active landslides can not only cross-validate the results, but also weaken the influence of SAR geometric distortions on landslide mapping in areas with steep topography with single-track SAR dataset.

Step 2: The 2D displacement rates and time series were calculated using the unwrapped interferograms from the identical SAR platform with different flight directions (i.e., ascending and descending Sentinel-1 images). Furthermore, for translational landslides, the 3D displacement rates and time series were further calculated with the same unwrapped interferograms by imposing a constraint on the surface parallel flow (Sun et al., 2016; Samsonov, 2019). The dominant movement directions of landslides were determined using the obtained 2D and 3D displacement maps and the geomorphological features that were obtained from DEM and optical images, including satellite and unmanned aerial vehicle (UAV) images.

Step 3: The optimal sliding direction for each pixel of the translational landslide was estimated using the InSAR-derived 3D displacement fields. Subsequently, the LOS measurements from different SAR platforms were transformed into the estimated sliding direction to achieve a unified datum of different SAR observations. Then, the unwrapped interferograms from different SAR platforms, which had identical flight directions (i.e., L-band ascending ALOS/PALSAR-1 and C-band ascending Sentinel-1 images) without overlap in the time domain, were linked to estimate the long-term displacement time series in the sliding direction using the Tikhonov regularization and singular value decomposition (SVD) methods. It is worth noting that an identical reference region was chosen for phase unwrapping to avoid systematic biases among the results from different SAR platforms.

Step 4: The displacement patterns and kinematic evolutions of landslides were investigated. The possible driving factors were determined for certain representative landslides based on the 2D and 3D displacement rates, time series, and hydrological factors including precipitation and water level fluctuation in the Jinsha River. Finally, unidimensional constitutive models of the rocks developed by laboratory creep testing (Aydan et al., 2014) were exploited to analyze the kinematic evolution and to determine the creep behavior of the landslide.

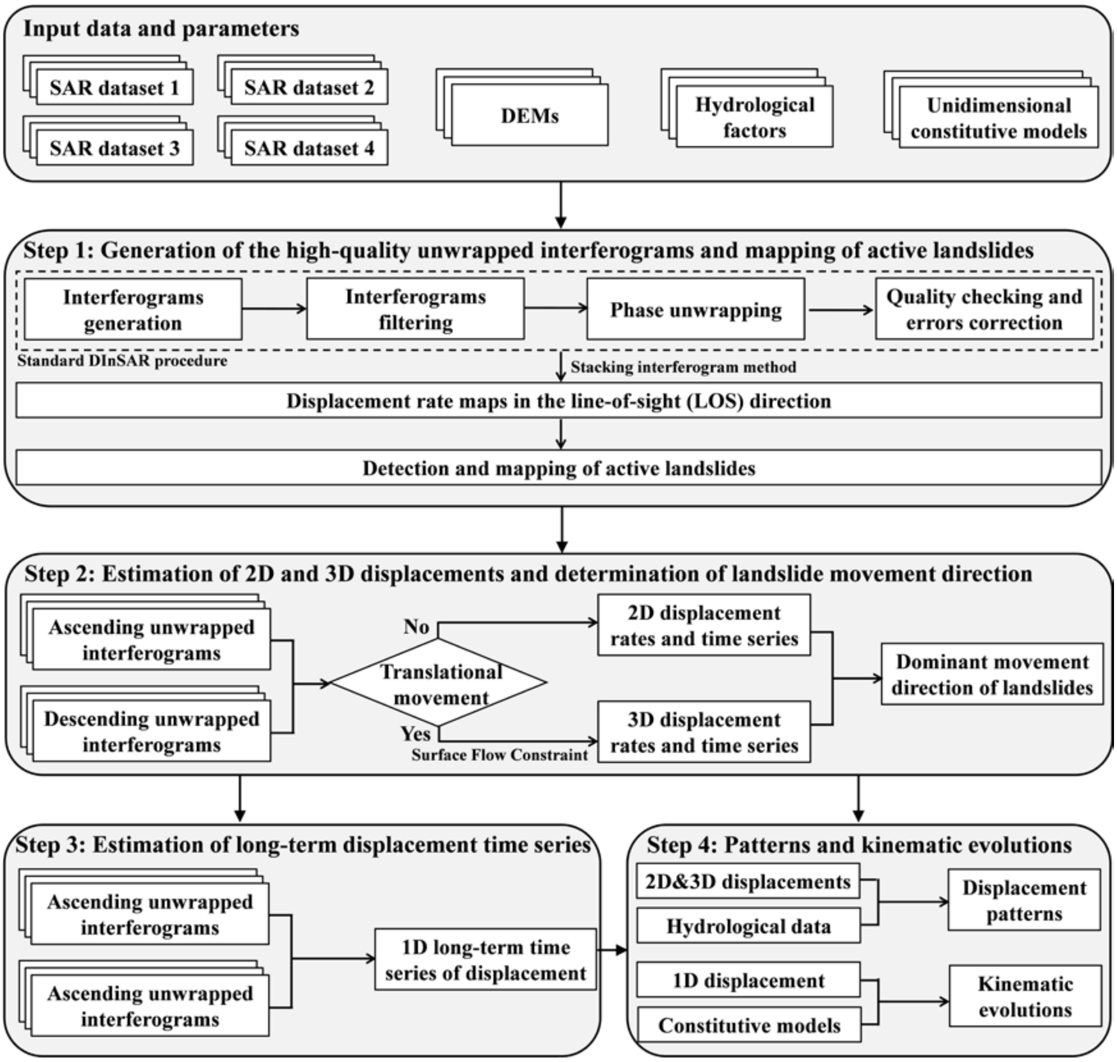

Fig. 4. Flowchart of 3D and long-term displacement time series estimation and mechanism analysis of landslide.

3.1 Inversion of two- and three-dimensional (2D and 3D) landslide displacement rates and time series

In general, InSAR satellites are insensitive to any movement along the azimuth direction (approximately in the north-south direction) as most SAR satellites operate in near-polar orbits (Samsonov et al., 2013). Therefore, for one specific landslide, if both ascending and descending SAR images are available with overlapping time intervals, the 2D displacement rates can be inverted using Eq. (1). This can be done based on the imaging geometry of SAR satellites by ignoring the displacement components in the north-south direction (Samsonov et al., 2014):

$$\begin{pmatrix}\hat{\boldsymbol{G}}\\ \boldsymbol{\Gamma}\end{pmatrix}\cdot\begin{pmatrix}V_E\\ V_U\end{pmatrix}=\begin{pmatrix}\hat{\boldsymbol{d}}\\ \boldsymbol{0}\end{pmatrix}, \tag{1}$$

where $\hat{\boldsymbol{d}}$ is the observation vector in the LOS direction from the ascending and descending tracks, V_E and V_U are the displacement rate parameters in the east-west and vertical directions, respectively; $\hat{\boldsymbol{G}}$ is the design matrix of observations consisting of east-west and vertical components of the LOS vector and time intervals between consecutive SAR acquisitions; and $\boldsymbol{\Gamma}$ is the Tikhonov matrix composed of the regularization parameter λ and regularization order L.

As 2D displacement parameter estimation from multi-platform SAR acquisitions is a rank-deficient and ill-posed inversion problem, Eq. (1) is built by imposing the Tikhonov regularization constraint to stabilize parameter inversion; additionally, it can also be built by imposing the additional constraint that the displacement time series have minimum acceleration (Pepe et al., 2016b). The unknown 2D displacement rates V_E and V_U in Eq. (1) can be estimated using SVD, and the 2D displacement time series are then retrieved through numerical integration of the time intervals between adjacent SAR acquisitions based on the estimated 2D displacement rates.

When the north-south displacement component cannot be neglected, it is necessary to retrieve 3D displacements. To date, several approaches have been explored to retrieve 3D displacements by combining multi-platform SAR observations as well as integrating DInSAR-based displacement results with external data, which includes combining of multi-track LOS and multiple aperture interferometry (MAI) measurements (Wright et al., 2004), fusion of the DInSAR and offset-tracking measurements (Hu et al., 2014a), combining multi-track offset-tracking measurements (Raucoules et al., 2013), integrating DInSAR and global navigation satellite system (GNSS) measurements (Samsonov et al., 2007), and using a priori information as a constraint (Gourmelen et al., 2011). Offset-tracking and MAI methods are challenging to map the displacement of slow-moving landslides owing to their low measurement precision. In the case that the SAR data sets from three different platforms are available and with distinctive flight directions and incidence angles, the 3D displacement rates and time series can be generated using a minimum acceleration approach (Pepe et al., 2016b). If only two independent SAR datasets from ascending and descending tracks are available, it is still possible to estimate the 3D landslide displacements by applying an a priori model about displacement process to reduce the free degrees. The surface-parallel flow model (Gourmelen et al., 2011) is an acceptable assumption in the displacement mapping of landslides.

For translational landslides, the movement direction is almost parallel to the ground surface under the effect of gravity (Varnes, 1996). Therefore, the surface–parallel displacement rate can be assumed as follows (Gourmelen et al., 2011; Sun et al., 2016):

$$V_U = (\frac{\partial H}{\partial x})V_E + (\frac{\partial H}{\partial y})V_N \quad , \tag{2}$$

where H is the elevation of the topography, and $\frac{\partial H}{\partial x}$ and $\frac{\partial H}{\partial y}$ represent the first derivatives in the east and north directions, respectively, which can be estimated using the external DEM. The sliding surface of a translational slide is an approximately regular plane, which is usually smoother than the external DEM (Frattini et al., 2018). Thus, prior filtering of the DEM often needs to be conducted to remove the effect of surface features on landslide displacement estimation. The 3D displacement inversion model can be constructed using Eqs. (1) and (2) (Samsonov, 2019):

$$\begin{pmatrix} \hat{\boldsymbol{G}} \\ \boldsymbol{H} \\ \boldsymbol{\Gamma} \end{pmatrix} \cdot \begin{pmatrix} V_N \\ V_E \\ V_U \end{pmatrix} = \begin{pmatrix} \hat{\boldsymbol{d}} \\ \boldsymbol{0} \\ \boldsymbol{0} \end{pmatrix} \quad , \tag{3}$$

where $\boldsymbol{H}$ is the constraint of surface–parallel flow and stands for $\left\{\frac{\partial H}{\partial y}, \frac{\partial H}{\partial x}, -1\right\}$; similarly, $\hat{\boldsymbol{G}}$ is the new design matrix of observations composed of the matrix G and north-south, east-west, and vertical components of the LOS vector; and V_N, V_E and V_U are the unknown displacement rates in the north-south, east-west, and vertical directions, respectively. Eq. (3) can be solved using the SVD method to obtain the 3D displacement rates, and the 3D displacement time series are then recovered through the numerical integration mentioned above.

3.2 One-dimensional long-term displacement time series estimation of landslide

To forecast the time of failure of a specific active landslide, it is of great significance to retrieve long-term (longer than 10 years) historical displacement time series by fusing multi-platform SAR observations. Assuming two independent SAR datasets S_1 and S_2 without overlap in the time domain, their SAR acquisition dates would be $\mathbf{T}_1 = \left[T_{1,1}, T_{1,2}, \cdots, T_{1,S_1}\right]$ and $\mathbf{T}_2 = \left[T_{2,1}, T_{2,2}, \cdots, T_{2,S_2}\right]$, respectively. The unwrapped interferograms of two SAR datasets with homologous highly coherent pixels, namely $\mathbf{d}_1 = \left[d_{1,1}, d_{1,2}, \cdots, d_{1,M_1}\right]$ and, $\mathbf{d}_2 = \left[d_{2,1}, d_{2,2}, \cdots, d_{2,M_2}\right]$ are linked to produce a long-term displacement time series, namely,

$\mathbf{D}=\left[D_1,D_2,\cdots,D_{T_1+T_2}\right]$, which spans all acquisition dates $\mathbf{T}_1+\mathbf{T}_2$ of the two SAR datasets. Moreover, all displacement time series are referred to as the earliest acquisition dates $T_{1,1}$.

InSAR measurements are a projection of the real 3D displacements of the earth's surface in the LOS direction of each SAR satellite, and SAR images from different satellites possess different wavelengths, incidence angles, and flight directions. Therefore, we should transform the LOS measurements from different SAR satellites to the unique sliding direction of the landslide based on the SAR imaging geometry and landslide geometry (Cascini et al., 2010). Here, we retrieved the optimal sliding direction for each pixel of the landslide using the InSAR-derived 3D displacements. In the monitoring of land subsidence, the time-gapped InSAR displacement time series from different SAR platforms can be linked using an a priori time-dependent model for the on-going displacements (Pepe et al., 2016a). However, for landslides it is difficult to find an a priori model that can exactly characterize the on-going slope displacements, since they are strongly controlled by external variables (e.g., rainfall, reservoir level, seismic events) that change the movement trends over time. Thus, in order to resolve the problem of rank deficiency caused by the time gap between two SAR datasets, we adopt the Tikhonov regularization method as follows (Tikhonov 1963):

$$\begin{bmatrix}\boldsymbol{G}\\ \boldsymbol{\Gamma}\end{bmatrix}\cdot\boldsymbol{m}=\begin{bmatrix}\boldsymbol{d}\\ \boldsymbol{0}\end{bmatrix} \quad , \tag{4}$$

where $\boldsymbol{G}=[\boldsymbol{G}_{S_1},\boldsymbol{G}_{S_2}]^{\mathrm{T}}$ is the design matrix consisting of time intervals between consecutive SAR acquisitions of two datasets, $\boldsymbol{d}=\left[\boldsymbol{d}_1,\boldsymbol{d}_2\right]^{\mathrm{T}}$ is the observations from two datasets, $\boldsymbol{m}$ represents the unknown displacement rate vector in the sliding direction of the landslide with the elements as $\left[m_0,m_1,m_2,\cdots,m_{T_1+T_2-1}\right]^{\mathrm{T}}$, and $\boldsymbol{\Gamma}$ is the Tikhonov matrix composed of regularization order L and regularization parameter λ, where the first-order regularization is adopted in this study. The optimal value of λ is estimated using the L-curve method (Hansen and O'Leary, 1993). Equation (4) can then be resolved based on the criterion of minimizing the objective function, as shown in Eq. (5):

$$\min(\|\boldsymbol{G}\boldsymbol{m}-\boldsymbol{d}\|_{L_2}^2+\|\boldsymbol{\Gamma}\boldsymbol{m}\|_{L_2}^2) \quad , \tag{5}$$

where $\|\cdot\|_{L_2}$ represents the Euclidean L_2 norm. Thus, the unknown displacement rate vector can be expressed as follows in Eq. (6), and the displacement time series is then reconstructed through numerical integration of the estimated displacement rates, as shown in Eq. (7):

$$\hat{\boldsymbol{m}}=(\boldsymbol{G}^{\mathrm{T}}\boldsymbol{G}+\boldsymbol{\Gamma}^{\mathrm{T}}\boldsymbol{\Gamma})^{-1}\cdot\boldsymbol{G}^{\mathrm{T}}\boldsymbol{d} \quad ; \tag{6}$$

$$D_{i+1} = D_i + m_i \Delta t_i, i = 0,1,2,\cdots,T_1 + T_2 - 1 \quad . \tag{7}$$

4 Displacement retrieval results and analyses

4.1 Line-of-sight (LOS) displacement rates between January 2007 and November 2018

The LOS displacement rate of each SAR dataset in the study area was independently calculated using the standard DInSAR procedure and stacking interferogram method (Lyons et al., 2003), as shown in Fig. 5. It is worth noting that the negative values (red color) represent the landslide moving away from the sensor, and the positive values (blue color) indicate movement towards the sensor. Dense measurement scatterers (MSs) with total numbers of 434927, 521529 and 551649 were identified from the ascending ALOS/PALSAR-1 (Fig. 5(a)), ascending Sentinel-1 (Fig. 5(c)) and descending Sentinel-1 (Fig. 5(d)) datasets respectively, producing an overall spatial density of greater than 2450 MSs/km^2 for the three SAR datasets. These scatterers were identified on the roads, buildings, and rocks and soils with sparse vegetation. In contrast, extremely sparse MSs of only 60798 were identified from ENVISAT dataset, generating an overall density of less than 400 MSs/km^2. Compared with other three SAR datasets, the incidence angle of the ENVISAT satellite was as small as 23°, thus causing severe geometric distortions (i.e., layover and shadow) of the SAR images (Wasowski and Bovenga, 2014), which result in extremely sparse MSs for landslide detection. As shown in Fig. 5, large-scale displacement regions were detected in the study area, and most displacement regions were greater than 2 km in length and/or width. For displacement rates calculated with ascending ALOS/PALSAR-1 (Fig. 5(a)) and ascending Sentinel-1 SAR images (Fig. 5(c)), the displacement regions and their extent were basically consistent, but the displacement magnitude and the detailed patterns were locally different across regions, likely due to the different wavelengths, imaging geometries, and acquisition durations between the two SAR datasets (see Table 1). Moreover, the locations of detected active displacement regions were generally consistent between ascending and descending Sentinel-1 measurements, but the extent of the displacement measured by ascending images was substantially greater than that of descending images (see Figs. 5(c) and (d)). This can be attributed to the slope orientation and the different sensitivities of landslide movement to the flight direction between ascending and descending SAR images. Therefore, we can combine both ascending and descending SAR images to map the complete extent of active landslides.

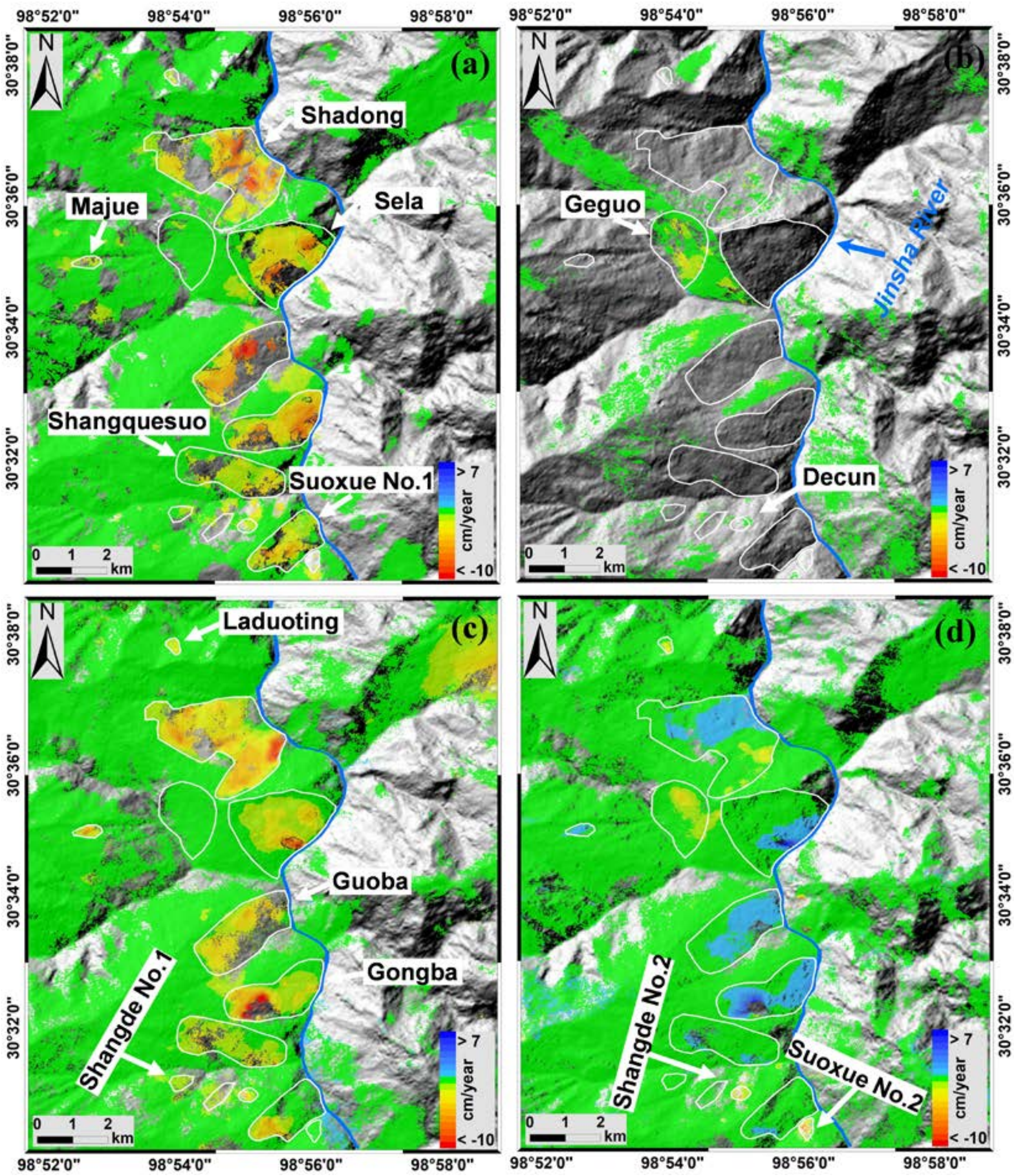

Fig. 5. Line-of-sight (LOS) displacement rate maps for the study area derived from (a) ascending ALOS/PALSAR-1 images between January 2007 and March 2011; (b) descending ENVISAT images between February 2007 and October 2010; (c) ascending Sentinel-1 images between August 2016 and October 2018; and (d) descending Sentinel-1 images between December 2016 and November 2018. The labels indicate the name of the detected landslides listed in Table 2, and the white solid polygons indicate the boundaries of the landslides.

Layover will be caused if the slope angle of the landslide is larger than the incidence angle of the SAR images, resulting in omissions for landslide detection. To avoid the effect of layover on the landslide mapping, we detected active landslides using a combination of the displacement rates derived from ascending ALOS/PALSAR-1, descending ENVISAT, and ascending and descending Sentinel-1 images, i.e., active landslides are first detected respectively using the displacement rates calculated with ascending

ALOS/PALSAR-1, descending ENVISAT, and ascending and descending Sentinel-1 images, and then the mapped landslides from each SAR dataset are mosaiced to produce the final landslide inventory map. The location and distribution of the detected active landslides are shown in Fig. 6, and detailed information is presented in Table 2. These landslides are situated at slope angles ranging from 10° to 51°, which can be attributed to the unique geological settings in the study area (Wang et al., 2000). Results from archived ALOS/PALSAR-1 and ENVISAT images indicate that these detected landslides have been active since January 2007. However, the spatiotemporal displacement characteristics of these landslides were inconsistent during different periods. For instance, the large displacement of the Shadong landslide mainly occurred in the middle and upper left regions between January 2007 and March 2011 and transferred to the lower right regions between August 2016 and October 2018, as shown in Figs. 5(a) and (c).

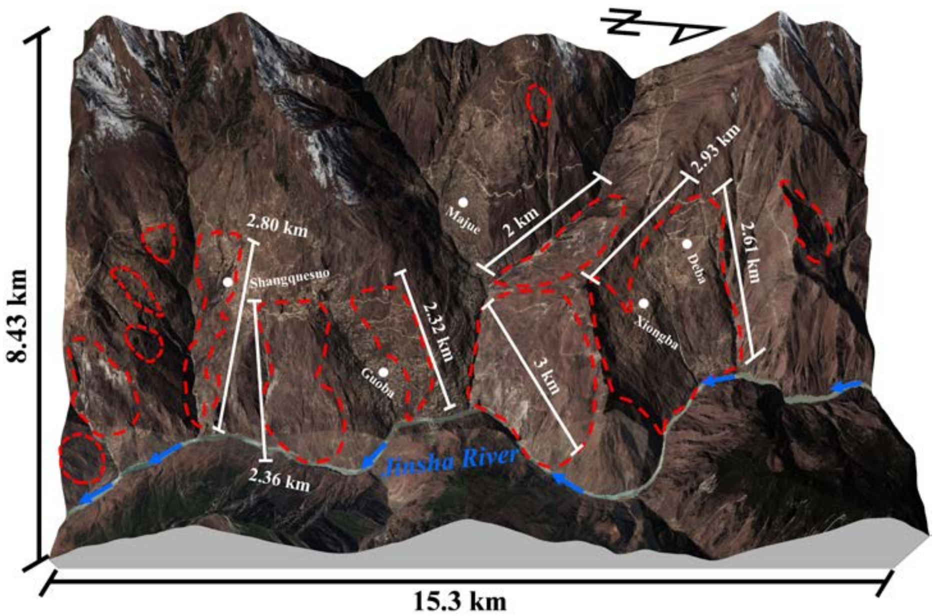

Fig. 6. Location and extent of the detected active landslides on the perspective remote sensing image. The points indicate the location of the main villages placed in the study area.

Table 2. Basic information of the detected landslides.

No.	Location Name	Aspect (°)	Slope (°)	Detected from SAR image	Dominant displacement
1	Laduoting	342	22–43	ALOS, S1A, S1D	Vertical and North
2	Shadong	32, 75	15–38	ALOS, S1A, S1D	Vertical, North and East
3	Sela	125	15–51	ALOS, S1A, S1D	East
4	Geguo	215	18–42	EV, S1D	South and West
5	Majue	70	20–38	ALOS, S1A, S1D	Vertical, North and East
6	Guoba	75	14–36	ALOS, S1A, S1D	East

7	Gongba	91, 110	10–35	ALOS, S1A, S1D	Vertical and East
8	Shangquesuo	140, 155	20–40	ALOS, S1A, S1D	East
9	Shangde No.1	60	15–34	ALOS, S1A	East
10	Shangde No.2	45	15–32	ALOS, S1A	North and East
11	Decun	350	14–34	ALOS, S1A, S1D	Vertical and North
12	Suoxue No.1	90	18–44	ALOS, S1A, S1D	Vertical and East
13	Suoxue No.2	349	22-38	ALOS, S1D	North and West

*Notes: ALOS and EV represent ALOS/PALSAR-1 and ENVISAT SAR images, respectively; and S1A and S1D stand for ascending and descending Sentinel-1 SAR images, respectively.

4.2 Two-dimensional displacement patterns of the detected landslides

One-dimensional LOS displacement results can be applied to determine the locations and spatial extents of landslides. However, it is challenging to accurately delimit the boundary of a landslide and determine its movement direction by merely using the LOS displacement results. Figure 7 shows the 2D displacement rate maps in the east-west and vertical directions of the detected landslides; the displacement rates were calculated using the method described in Section 3.1, where the positive values (blue color) indicate eastward movement and the negative values (red color) indicate westward movement in the horizontal component map (Fig. 7(a)), and the negative values (red color) represent the downward movement and the positive values (blue color) represent upward movement in the vertical component map (Fig. 7(b)). The maximum east-west displacement rate is greater than 8 cm/year, and the maximum vertical displacement rate is less than -7 cm/year. In general, the displacement and failure patterns of landslides are subject to topography, lithology, and geological structure of slopes, as well as external driving factors, such as earthquakes and rainfall. From Fig. 7, we can see that each detected landslide has its own movement direction and displacement pattern. All the detected landslides except the Laduoting, Geguo and Suoxue No.2 landslides are moving eastward, whereas the Laduoting landslide is moving northward and the Geguo and Suoxue No.2 landslides are moving westward. It is worth noting that, evidence from optical image (Fig. S3) illustrates that the main movement direction of the Laduoting landslide is along the north-south direction, thus failing to measure its movement by the east-west displacement map presented in Fig.7 (a). Moreover, most landslides are dominated simultaneously by horizontal and vertical movements, such as the Laduoting, Shadong, Majue, Gongba, Decun, and Suoxue No.1 and No.2 landslides (see Table 2), and some landslides are dominated by horizontal movement, such as the Sela and Geguo landslides (see Table 2).

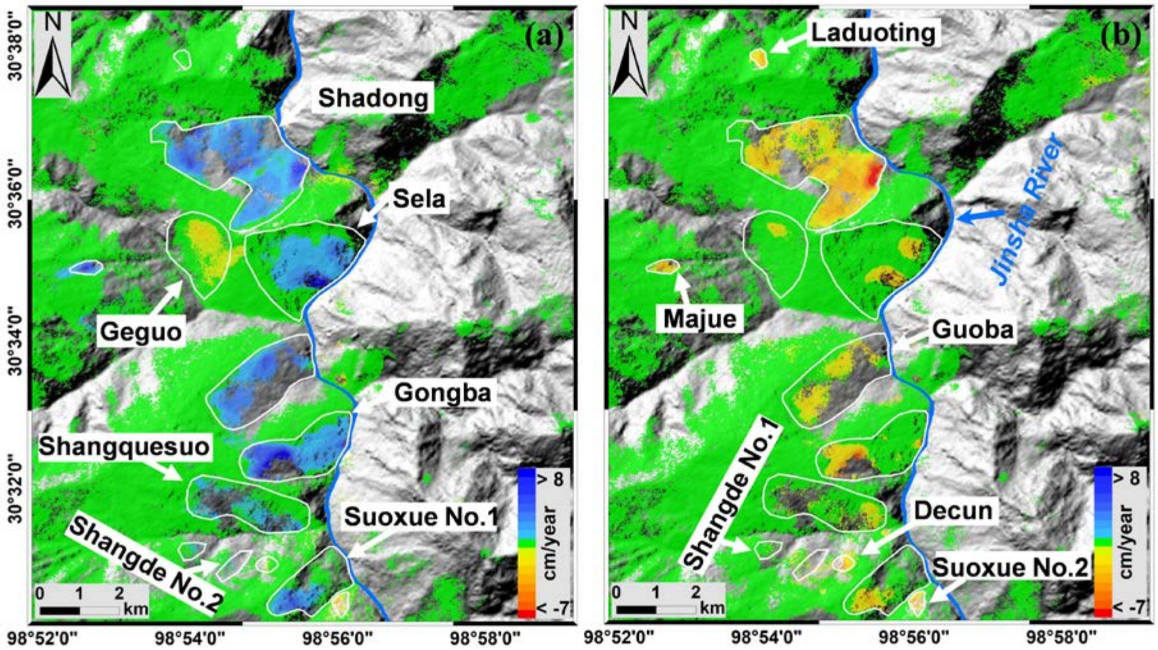

Fig. 7. Two-dimensional displacement rate maps of the detected landslides from December 2016 to October 2018 calculated with ascending and descending Sentinel-1 images. The white solid polygons indicate the boundaries of the landslides. (a) Horizontal east-west displacement rate map; and (b) vertical displacement rate map.

4.3 Three-dimensional displacement characteristics of the Shadong landslide

It is necessary to retrieve the 3D displacement rates and time series of landslides if the north-south displacement cannot be neglected. We take the Shadong landslide located at the outside of a meander bend of the Jinsha River, as an example to retrieve its 3D displacement rates and time series using the method described in Section 3.1. Field geological exploration (Fig. 2(c)) revealed that the landslide can be classed as a translational slide according to Cruden and Varnes (1996) classification. Figure 8(a) shows the optical remote sensing image of the Shadong landslide acquired in March 2015. The extent of the landslide is ~2.61 km in length and ~2.93 km in width. The polygons with different colors in Fig. 8(a) indicate different blocks (i.e. B1-B5) of the landslide, which are divided according to the geomorphological analysis and the developments of the gullies (see Section 2.1). The 3D displacement rates in the north-south, east-west, and vertical directions from December 2016 to October 2018 are shown in Figs. 8(b), (c), and (d), respectively. The positive values (blue color) indicate northward movement and the negative values (red color) indicate southward movement in Fig. 8(b). The maximum displacement rates in the north-south, east-west, and vertical directions were more than 80, 76, and -67 mm/year, respectively. We then extracted the displacement rates and elevation along two representative Profiles AA’ and BB’ (see Fig. 8(d)) to reveal the detailed spatial displacement characteristics, as shown in Fig. 9. The error bars in Fig. 9 indicate the standard deviations of the estimated 3D displacement rates. Profile AA’ is approximately parallel to the main sliding direction of block B1, and Profile BB’ transversely passes through blocks B1-B4. Furthermore, the optimal sliding direction for each pixel of the landslide was calculated using the estimated 3D displacement rates, as shown in Fig. 10.

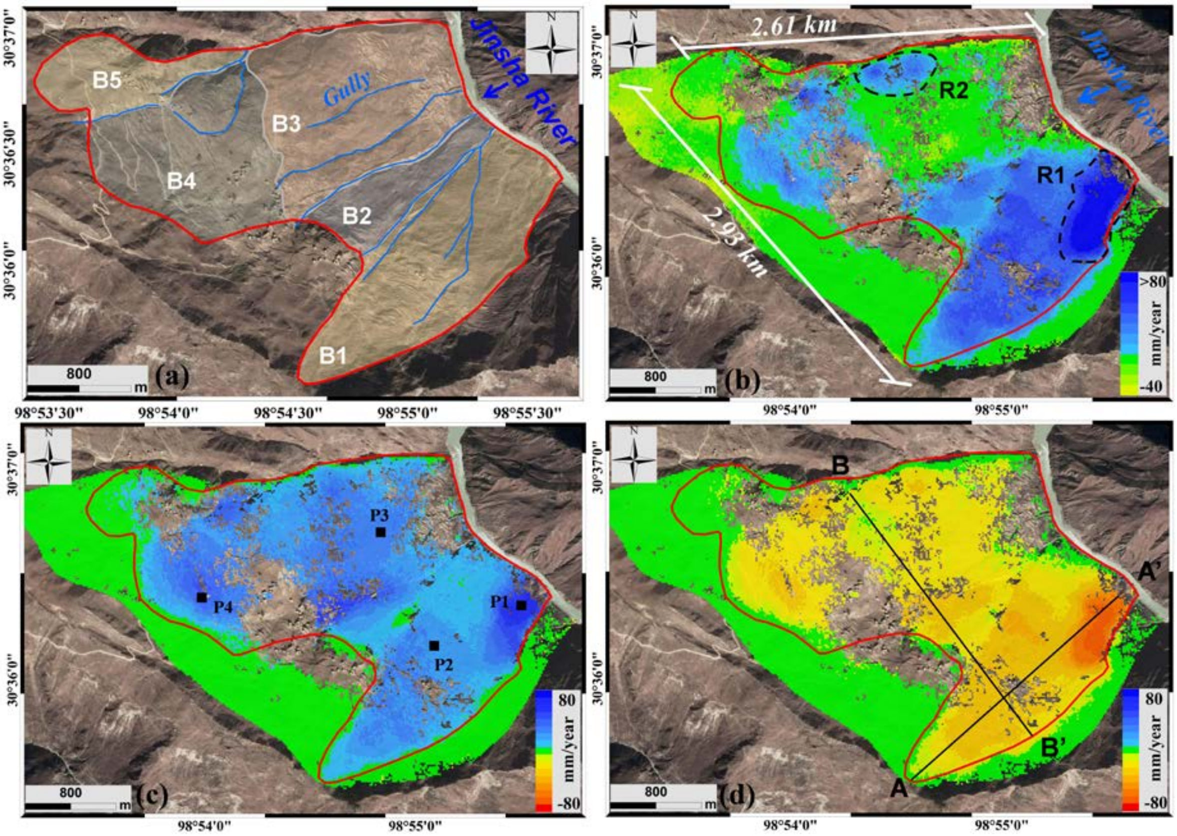

Fig. 8. Remote sensing image and 3D displacement rate maps from December 2016 to October 2018 of the Shadong landslide. The boundary of the landslide movement is marked using the red solid lines, and the black dotted polygons (i.e., R1 and R2) in (b) indicate the two secondary sliding regions. (a) Remote sensing image acquired in March 2015, where different colors represent five blocks of the landslide; (b) north-south displacement rate map; (c) east-west displacement rate map, from which Points P1–P4 are analyzed in the text to show displacement time series; and (d) vertical displacement rate map, where two black lines indicate the locations of Profiles AA’ and BB’.

As shown in Figs. 8, 9, and 10, the 3D displacement map provides an intuitive description of the displacement characteristics and movement direction of each block of the Shadong landslide, which can be further used to analyze the displacement characteristic and failure mode on a detailed scale. In particular, the displacement characteristic obtained from the 3D displacement results exhibit strong agreement with the actual geomorphological features of the slope observed from satellite and UAV images (see Figs. 8 and S1), presenting the characteristics of block displacement. The north and vertical displacement rates on blocks B1–B2 are larger than those on blocks B3–B4. In contrast, the east-west displacement rates of blocks B1–B2 are slightly lower than those of blocks B3–B4, except at the lower-right part of block B1. From the 3D displacement results shown in Figs. 8(b), (c), and (d), we can clearly see a distinct sliding boundary between block B1 and block B2. As evidenced in the east-west and vertical displacement rate maps shown in Figs. 8(c) and (d), the entire landslide shows a trend of eastward and downward movement. However, evidence from Figs. 8(b) and 9 suggests that the northward displacement mainly occurred in blocks B1, B2 and B4, and there is no remarkable north-south displacement in the block B3 except for a small region on its left side (i.e., R2 labelled in Fig. 8(b)). The geomorphological feature and optical image (Fig. S1(a) and (b)) demonstrate that the Region R2 is a secondary sliding area on the block B3, and it moves mainly to the north direction. Furthermore, geomorphological analysis and slope aspect indicate that blocks B1, B2 and B4 are moving toward the northeast direction, and blocks B3 is moving toward the east direction, as described in detail in Section 2.1.

In Fig. 9(a), the 3D displacement rates of block B1 (along profile AA') are negatively correlated with the elevation, that is, the displacement at the lower section is larger than that at the middle-to-upper section. This evidence indicates that block B1 belongs to a pull-type landslide (Lu, 2015), which can be adequately verified by the displacement boundary presented in Fig. 8 and the geomorphological feature presented in Fig. 10, that is, the displacement boundary of block B1 is shaped like a tower, and the lateral width of the head is smaller than that of the foot. A similar type of landslide has previously been identified in the Wudongde reservoir area in the lower reaches of the Jinsha River (Zhao et al., 2018). Moreover, the displacement rate in the north direction of block B1 is also larger than that in the east and vertical directions, which suggests that block B1 mainly moves toward the north.

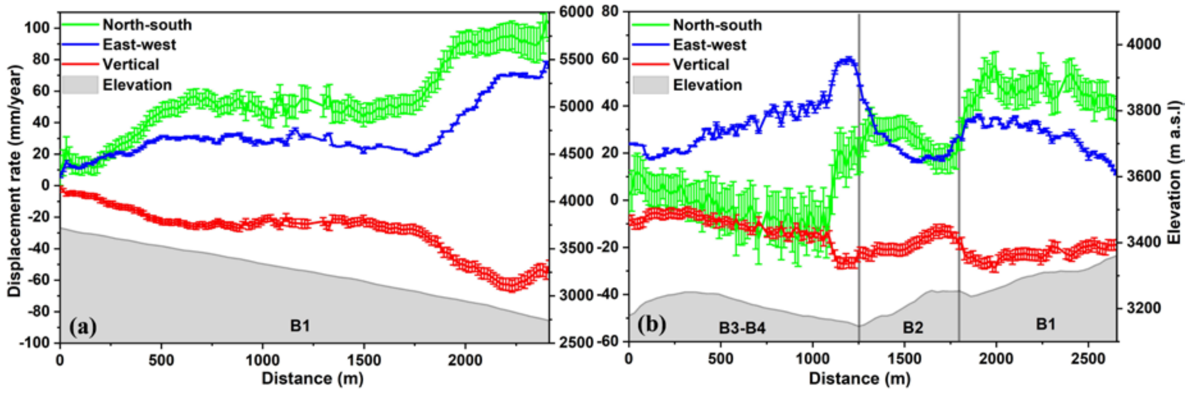

Fig. 9. Displacement rates along the three components and elevation along the Profiles AA' and BB' labeled in Fig. 8(d). (a) Profile AA'; and (b) Profile BB', where B1, B2 and B3–B4 indicate block 1, block 2 and blocks 3-4 of the Shadong landslide labeled in Fig. 8(a), respectively.

The largest displacement rates were observed at the leading edge of block B1, that is, Region R1 marked in Fig. 8(b). The movement direction of each pixel is shown in Fig. 10(b), and the 3D displacement rate maps are presented in Fig. 11. The boundary of the maximum displacement region can be clearly seen in Fig. 11, where the 3D displacements are precisely bounded by the cracks and scarp. The region moves toward the Jinsha River with maximum displacement rates of approximately 125, 75, and -40 mm/year in the north, east, and vertical directions, respectively. The displacement in the north direction was significantly larger than that in the east and vertical directions as the slope faced north (see Figs. S1 and 11(a)). Region R1 is the most active area on the entire Shadong landslide, where a main scarp has formed at the back edge of the region, and two continuous, large cracks have also developed on the left and right sides of the region (see Figs. S1(e), (f) and 11). These displacement and geomorphological features are completely consistent with the failure modes I and III of pull-type landslide derived from the theoretical analyses of geologist (Lu, 2015). Thus, it can be concluded that block B1 are deforming along the entire weak face under the control of the mechanical behaviors (strain and shear stress) of geo-materials, and the shear deformation occurs in the Region R1 under the effects of external driving factors (e.g., water level fluctuations in the Jinsha River, see Section 5.2).

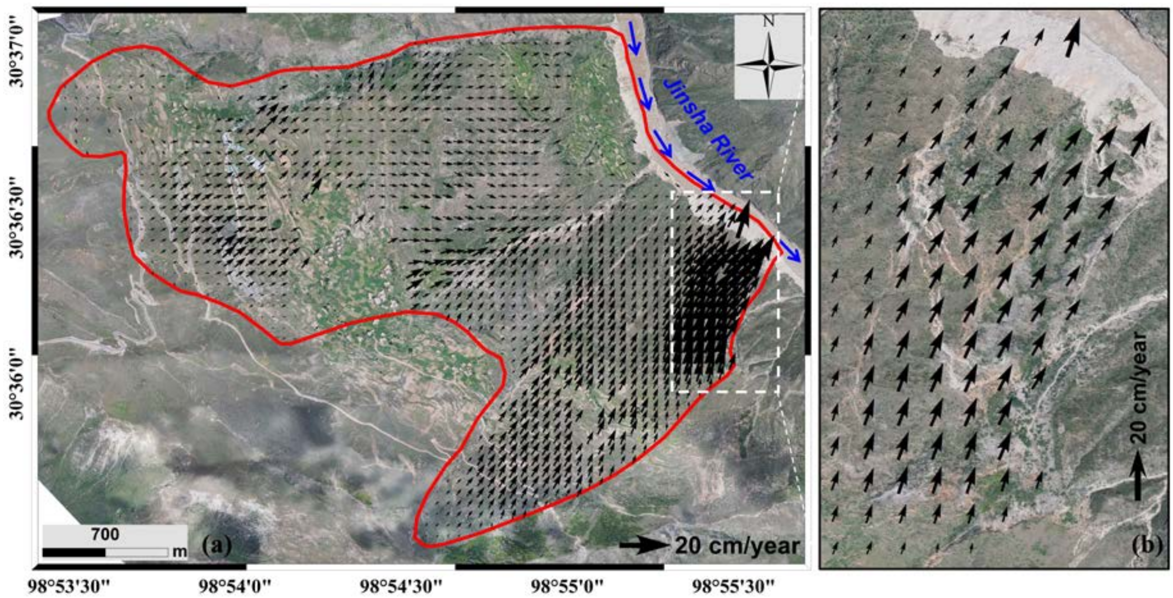

Fig. 10. (a) The horizontal movement vector of the Shadong landslide; and (b) the enlarged horizontal movement vector over Region R1 marked in Fig. 8(b). The base map is the UAV image acquired on 13 June 2020, with a spatial resolution of 0.3 m.

In Fig. 10, the sliding directions show that the block B3 moves eastward, and the block B4 moves northward and eastward, which is highly consistent with the actual geomorphic features of blocks B3 and B4 (see the details in Section 2.1). Geomorphological analyses of optical images and shaded relief map suggest that the slope aspect of block B3 mainly faces to the east, and the slope aspect of block B4 mainly faces to the northeast, see the details in Section 2.1 and Figs. 2(b) and S1.

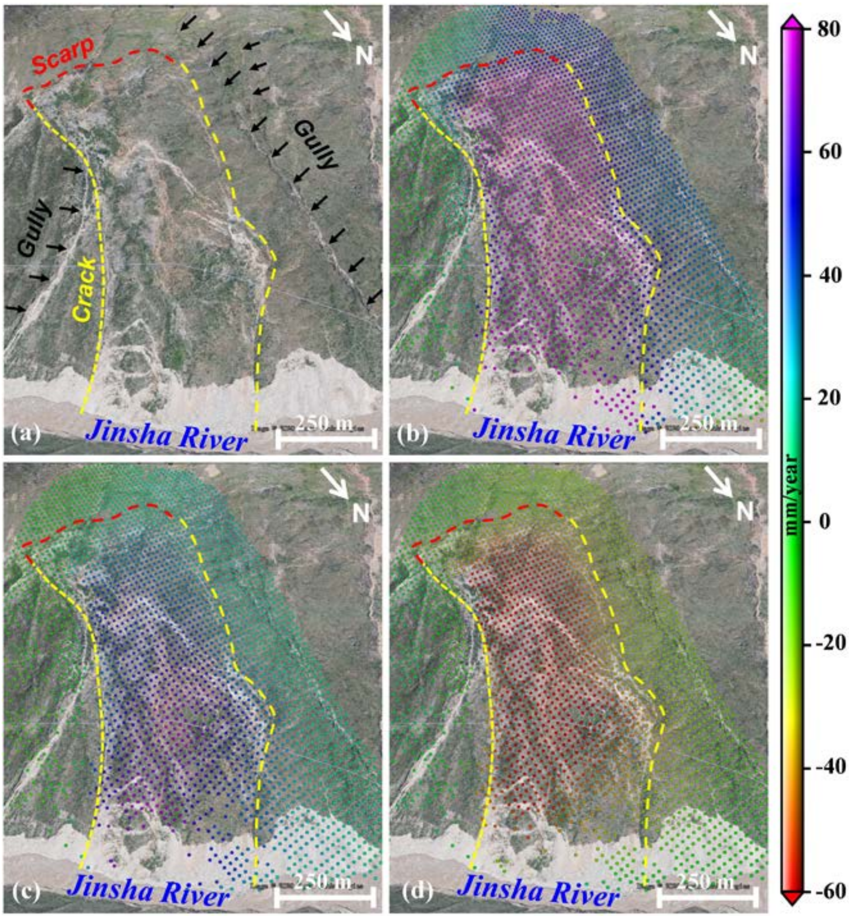

Fig. 11. Three-dimensional displacement rate maps of Region R1 marked in Fig. 8(b). (a) UAV image acquired on 13 June 2020; (b) north-south displacement rate; (c) east-west displacement rate; and (d) vertical displacement rate.

To investigate the temporal evolution of the landslide displacements, we selected four typical points (P1–P4 in Fig. 8(c)) located in different parts of the Shadong landslide to exhibit their 3D displacement time series. Points P1 and P2 are located on block B1, and Points P3 and P4 are located on blocks B3 and B4, respectively. Figure 12 shows the displacement time series along the three main components (i.e., north, east, and vertical directions) for Points P1–P4 from December 2016 to October 2018. We can see that the largest cumulative displacement that occurs at Point P1 was approximately 157, 116, and -98 mm in the north, east, and vertical directions, respectively, and it corresponds to the fastest moving area (Fig. S1). Meanwhile, a larger cumulative displacement was also observed at Points P2 and P4, with cumulative displacements of 89, 43, and -49 mm for Point P2 and 84, 97, and -50 mm for Point P4 in the north, east, and vertical directions, respectively. Point P3 showed relatively small cumulative displacements as -7.3, 60.5, and -24.8 mm in the north, east, and vertical directions, respectively. Field geological exploration evidenced that there is a major locked segment in the area where Point P3 is located (Fig. 2(c)), and it controls the deep-seated stability of the Shadong landslide (Li et al., 2021). Points P1, P2 and P4 showed an approximately linear displacement trend in the three directions during the InSAR observation period from December 2016 to October 2018; and Point P3 exhibited a roughly linear movement trend, and there are short periods of acceleration displacement signal in some SAR acquisitions. Furthermore, the displacement time series along the three main components revealed that the temporal evolution of the displacement of the four points was inconsistent. The cumulative displacement of Points P1 and P2 in the north direction was larger than that in the east and vertical directions. In contrast, the displacement in the north direction of Points P3 and P4 is smaller than that in the east and vertical directions.

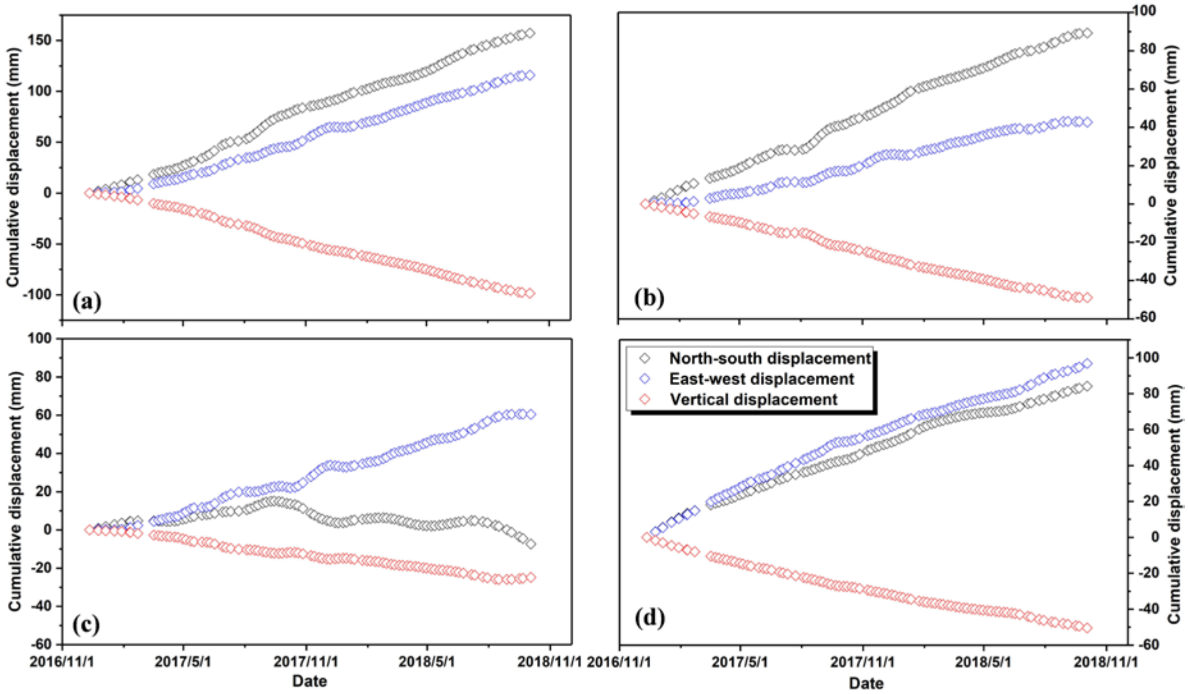

Fig. 12. The displacement time series along the three main components for Points P1–P4 (marked in Fig. 8(c)) of the Shadong landslide from December 2016 to October 2018. (a) P1; (b) P2; (c) P3; and (d) P4.

4.4 Long-term displacement time series in the sliding direction of the Shadong landslide

To generate long-term displacement time series in the sliding direction of the Shadong landslide over ten years, we link the L-band ALOS/PALSAR-1 measurements acquired between January 2007 and March 2011 and the C-band Sentinel-1 measurements acquired between October 2014 and October 2018 with a four-year gap based on the method described in Section 3.2. First, we resampled the high-quality unwrapped interferograms from the ALOS/PALSAR-1 and Sentinel-1 images to a common georeferenced grid with the uniform spatial resolution of 15 m, and the common measurement scatterers among the two datasets were selected for further processing. Then, the resampled interferograms in the LOS direction of the Sentinel-1 and ALOS/PALSAR-1 images were transformed into the estimated sliding direction of the slope (Fig. 10).

Subsequently, the long-term displacement time series was estimated using Eq. 4. Meanwhile, the long-term time series of displacements were also calculated using the least squares (LS) and linear fitting methods, respectively, to highlight the performance of the proposed method.

Figure 13 shows the long-term displacement time series of Points P1–P4 (marked in Fig. 8(c)) of the Shadong landslide, where the red triangles indicate the displacements calculated with the proposed method (i.e., Tikhonov regularization), the blue rectangles indicate the ones calculated using the LS method, and the gray solid circles are the ones calculated by the linear fitting method. We can see that the results obtained by the LS method exhibit a serious deviation compared with those obtained by the proposed method and the linear fitting method for the sake of rank deficiency problem. This suggests that the long-term displacement time series results generated by the LS method are unreliable to some extent (Pepe et al., 2016a). Comparison of the results derived from the Tikhonov regularization and linear fitting methods, the displacement time series results generated by the two methods are relatively close at Points P1 and P3; however, there is a large deviation at Points P2 and P4, which will be discussed in detail in Section 5.2. Here the results from the Tikhonov regularization method are finally selected to investigate the movement characteristics of the Shadong landslide over the past nearly 12 years. Results show that all points exhibit creep displacement characteristics, among which the fastest movement was measured in Region R1 marked in Fig. 8(b), and the cumulative displacement in the sliding direction at Point P1 was around -1.33 m between January 2007 and October 2018. The smallest cumulative displacement was measured at Point P4 with a magnitude of approximately -0.56 m. In addition, some large cumulative displacements were also observed at Points P2 and P3, with magnitudes of around -0.97 and -0.8 m, respectively. A significant signal of the displacement acceleration was observed at Points P1, P2, and P3 from January 5 to May 22, 2008, which may be exactly correlated with the Wenchuan earthquake in Sichuan, China, on May 12, 2008 (Yin et al., 2009). Furthermore, we can see from Fig. 13 that Points P1, P2, P3, and P4 experienced a nonlinear displacement trend during the period from January 2007 to October 2018. The movement rates of Points P2 and P3 before October 10, 2009, were faster than those after October 10, 2009, and the slight acceleration signals of the displacement were detected at Points P1 and P4 on July 21, 2016. Thus, it is essential to conduct continuous displacement monitoring with newly acquired SAR images or ground-based equipment, such as GNSS or crack gauges.

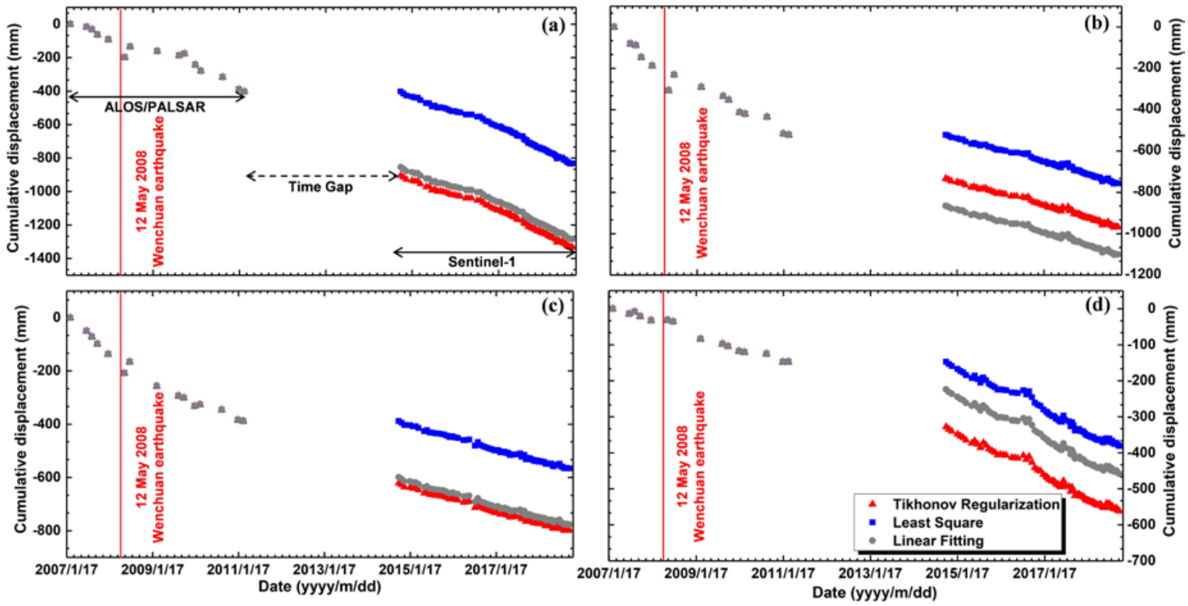

Fig. 13. One-dimensional long-term displacement time series in the sliding direction of the Shadong landslide for Points P1–P4 calculated by fusing L-band ALOS/PALSAR-1 and C-band Sentinel-1 SAR measurements from January 2007 to October 2018. (a) P1; (b) P2; (c) P3; and (d) P4.

5 Discussion

5.1 Kinematic evolution and creep behavior of the Shadong landslide

To assess the long-term stability and forecast the time of failure of an active landslide, it is important to investigate its long-term kinematic evolution and creep behavior. Previous studies (Fukuzono, 1985; Intrieri et al., 2019; Saito, 1969; Aydan et al., 2014) have demonstrated three stages (also sometimes known as displacement-time curve) of the kinematic evolution and creep behavior of slopes before failure, as shown in Fig. 14(a). The first stage is the primary creep (or transient or decelerating) with the displacement rate logarithmically decreasing, followed by the second stage of secondary creep (or constant-state) with a steady displacement rate. After a period of relative stability within the second stage, the third stage of tertiary creep (or hyperbolic acceleration) begins, and the slope either accelerates until it ruptures (or fails) (A) or accelerates and then reaches a new limit equilibrium (B), as shown in Fig. 14 (a). The results from laboratory creep testing of rocks (Aydan et al., 2014) have demonstrated that such the three stages can be characterized using unidimensional constitutive laws/models of the rocks, as illustrated in Eqs. (8)-(10). In these equations, Eq. (8) is applicable to primary stage, hereinafter refer as Lomnitz 1956, 1957; Eq. (9) is applicable to primary and secondary stages, hereinafter refer as Modified Lomnitz law; and Eq. (10) is applicable to all stages creep terminating with rupture, hereinafter refer as Aydan et al. 2003.

$$S = A \cdot \ln(1+\alpha t) \quad \text{(Lomnitz 1956, 1957)} \tag{8}$$

$$S = A + B \cdot \log(t) + C \cdot t \quad \text{(Modified Lomnitz law)} \tag{9}$$

$$S = A \cdot (1 - e^{-t/\tau_1}) + B \cdot (e^{t/\tau_2} - 1) \quad \text{(Aydan et al. 2003)} \tag{10}$$

where S indicates the displacement, A, B, α, C, τ_1 and τ_2 are constants, and t is the time.

To investigate the kinematic evolution and creep behavior of the Shadong landslide, we applied unidimensional constitutive laws of the rocks to model the displacement behavior of Points P1 and P3 marked in Fig. 8(c). The displacement time series of Points P1 and P3 were modelled based on Eqs. (8), (9) and (10) using the Levenberg-Marquardt algorithm (Marquardt, 1963), respectively. The original InSAR observations, the modelled displacement and the residuals are plotted in Fig. 14, and comparison of the results modelled by different unidimensional constitutive laws is presented in Table 3. For Point P1, the displacement modelled by Modified Lomnitz law perfectly matches that observed by ALOS/PALSAR-1 and Sentinel-1 images (see Fig. 14(b)), with a correlation coefficient (R) of 0.997. Nevertheless, the laws of Lomnitz 1956, 1957 and Aydan et al. 2003 failed to model the displacement of Point P1, because Eqs. (8) and (10) cannot be converged when they were used to model the displacement of Point P1. Similar to Point P1, the law of Aydan et al. 2003 also failed to model the displacement of Point P3, but it can be perfectly modelled by the laws of Lomnitz 1956, 1957 and Modified Lomnitz (see Fig. 14(c)), with the correlation coefficients (R) of 0.999 and 0.996, respectively. Evidences from Table 3 and Fig. 14(c) suggest that the displacement modelled by Lomnitz 1956, 1957 is closer to InSAR observations than that modelled by Modified Lomnitz law, i.e., there are higher correlation coefficient and smaller mean of the residuals in the modelled results from Lomnitz 1956, 1957. Moreover, from Figs.14 (b) and (c), we can see that the cumulative displacement of Point P1 is much larger than that of Point P3. During the period of January 2007 to October 2018, the temporal evolution of Point P1 showed an overall linear trend, whilst Point P3 was deforming in a non-linear trend with the logarithmically decreasing rate. Based on the modelled results of the unidimensional constitutive laws of rocks, in conjunction with the temporal evolution behaviours of Points P1 and P3, it can be concluded that the slope movement at Point P1 may be in the second stage (secondary creep), while the slope movement at Point P3 may be in the first stage (primary creep). The three stages of creep behavior of slopes can be broadly organized into two categories (Lu, 2015): stable feature (primary and secondary creeps) and unstable feature (tertiary creep). As a consequence, the results suggest that the Shadong landslide exhibits the stable feature currently. In addition, we can see from Figs. 14(d) and (e) that the maximum residual appears on the SAR observation on May 22, 2008 (see the red dotted ellipses). This finding further supports the conclusion that the 2008 Wenchuan earthquake resulted in a transient acceleration in landslide displacement.

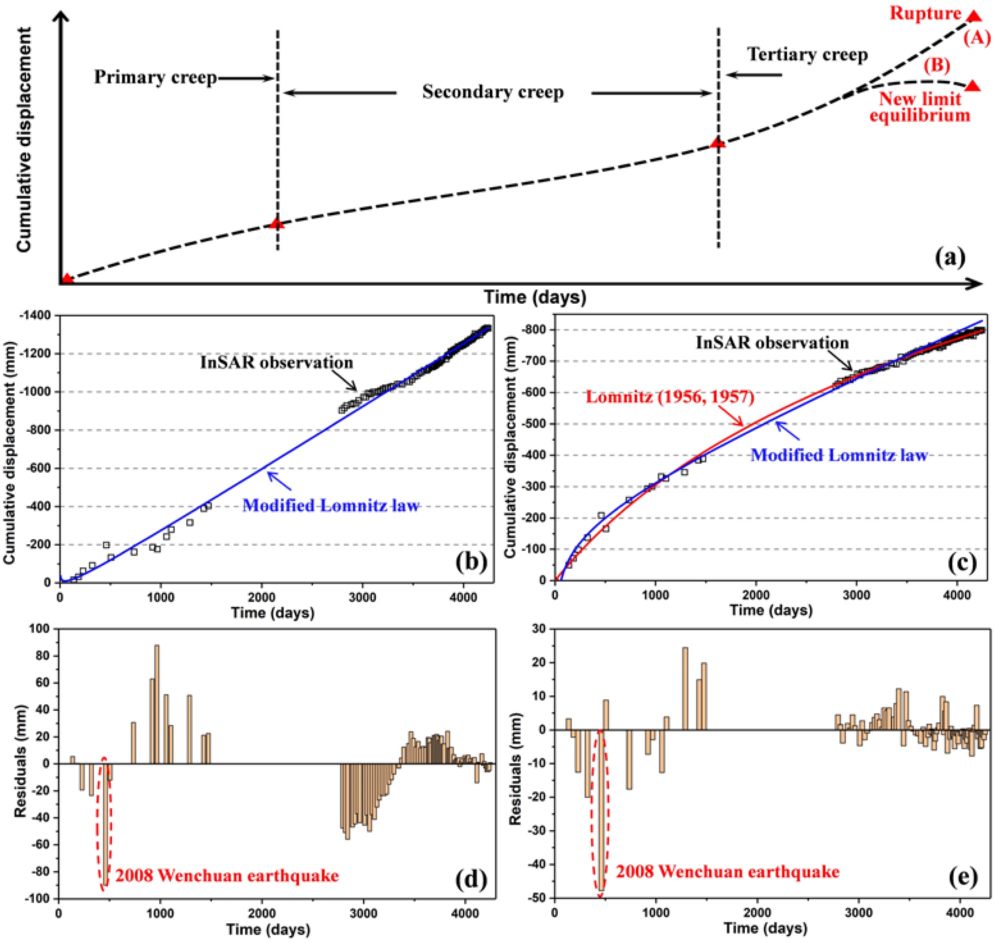

Fig. 14. Kinematic evolution and creep behavior of the Shadong landslide from January 2007 to October 2018. (a) Standard three-stage creep rupture curve of the slope (modified after Fukuzono, 1985; Intrieri et al., 2019; and Saito, 1969); (b) displacement time series (in the sliding direction) of the Shadong landslide for Point P1 derived from InSAR observations (black squares) versus that derived by modeling of rock's unidimensional constitutive laws (blue curve); (c) displacement time series of Point P3 derived by InSAR observations (black squares) versus that derived by modelling (red and blue curves); (d) Residuals of Point P1, calculated by subtracting the modeled values (using Modified Lomnitz law) from the observed values; (e) Residuals of Point P3, calculated by subtracting the modeled values (using Lomnitz 1956, 1957) from the observed values. The locations of Points P1 and P3 are marked in Fig. 8(c).

Table 3 Comparison of the results modelled by different unidimensional constitutive laws

Points	Models/Laws	Convergence of the solution	R	Mean of residuals (mm)	Standard deviation of residuals (mm)
P1	Lomnitz 1956, 1957	No	-	-	-
	Modified Lomnitz law	Yes	0.997	18.8305	18.6

	Aydan et al. 2003	No	-	-	-
	Lomnitz 1956, 1957	Yes	0.999	4.8357	6.5
P3	Modified Lomnitz law	Yes	0.996	7.0208	6.1
	Aydan et al. 2003	No	-	-	-

5.2 Performance of the proposed method for estimating the long-term landslide displacement

Some researchers (Pepe et al., 2016a; Wu et al., 2020) have explored the use of geotechnical models to link time-gapped InSAR displacement time series that derived from different SAR sensors (e.g., ENVISAT and COSMO-SkyMed), thus estimating the long-term time series (> 10 year) of land settlement. The outcomes obtained in Section 5.3 clearly show that the long-term displacement time series of the Shadong landslide calculated with the proposed method can be well modelled by the unidimensional constitutive laws of rocks. As there are no ground-based measurements of displacements, we regard the modelled displacement results of rocks' unidimensional constitutive laws as references to assess the performance of our proposed method. Apart from the Points P1-P4 marked in Fig. 8(c), six points (PS1-PS6) located in different areas of the Shadong landslide were further selected to exhibit the long-term displacement time series. The locations of Points PS1-PS6 are marked in Fig. S4, and the long-term displacement time series derived from the Tikhonov regularization, linear fitting and LS methods are given in Fig. S5. Furthermore, we exploited the unidimensional constitutive laws of rocks (Eqs. (8)-(9)) to model the displacement time series generated by Tikhonov regularization and linear fitting methods, respectively. Fig. S6 shows the displacement time series of Points P1-P4 and Points PS1-PS6 estimated from the Tikhonov regularization method (black squares) and rocks' unidimensional constitutive models (blue curves), and Fig. S7 shows the ones estimated from the linear fitting method (black squares) and rocks' unidimensional constitutive models (blue curves). In addition, a quantitative comparison of the modelled displacement results is presented in Table S1. As can be seen from Figs. S6 and S7, the long-term displacement time series estimated with the Tikhonov regularization method overall outperform those estimated with the linear fitting method, in which the rocks' unidimensional constitutive laws modelled the displacement time series of each point estimated from the Tikhonov regularization method very well. In contrast, in some measurements generated by the linear fitting method, such as Points P4 and PS2 in Fig. S7, the rocks' unidimensional constitutive laws did not model the displacement time series very well. Moreover, from the standard deviations (STDs) of the residuals (calculated by subtracting the modeled values from the InSAR measured values) listed in Table S1, we can see that the STDs of the Tikhonov regularization method are generally smaller than those of the linear fitting method. These evidences can verify the validity of our proposed method to some extent. It is worth to specify that, the unidimensional constitutive laws presented in Eqs. (8)-

(9) were developed under the natural movement state of the rocks (Aydan et al., 2014), i.e., there is no intense and sudden disturbances from external environmental factors such as strong earthquakes. Similarly, our method is suitable for retrieving the long-term displacements of slopes which are moving naturally under the effect of gravity. However, the generated results may be biased in the case that the landslides exhibit strong non-linear movement trends or transient acceleration displacement signals caused by periodic strong rainfall or strong earthquake events.

5.3 Possible driving factors for the landslide displacement

Gravity is usually the primary driving factor for landslide displacement. In addition, several external environmental factors can contribute to the acceleration of landslide displacement, such as heavy precipitation, groundwater and river level fluctuations, and earthquakes. To investigate the possible driving factors for landslide displacement in this case, we selected six points (Points P5–P10) located in different regions of four massive landslides to analyze the correlations between displacement and environmental factors. Figure 15(a) shows an optical image of four massive landslides and six locations, and the optical images of these landslides are enlarged in Fig. S8 to clearly show evidences of their activity. The analysis of the optical images reveals that there have been cracks, collapses and scarps developed on the surface of these slopes. Points P5, P7, and P9 are located near the intersection of the slope and the watercourse of the Jinsha River, and Points P6, P8, and P10 are located far away from the Jinsha River. Figures 15(b)–(g) show the 2D displacement time series in the east-west and vertical directions of Points P5–P10 and the monthly precipitation in the study area.

Figure 15 demonstrates that heavy precipitation mainly occurred from June to September each year (i.e., in the summer) in the study area. In particular, the number of days with rainfall during this period was much greater than in other periods. Heavy precipitation may have accelerated the displacement of landslides in two ways. First, the stability of the landslide may have been directly reduced, that is, regional increases in the duration, intensity and amount of rainfall can generate elevated pore-water pressures of the slope, thus resulting in a decrease in the shearing strength of the soil and an increase in displacement (Handwerger et al., 2019). Second, the displacement of landslides may be indirectly accelerated as follows: periodic rainfall generally causes fluctuations in the Jinsha River water level, which reduces shear stress in the foot of the landslide and further decreases the safety factor (FS); this increases its instability (Shi et al., 2015; Lacroix et al., 2020). As shown in Fig. 15, the landslide displacements at Points P5, P7, and P9 showed a strong correlation with monthly precipitation, while there was a weak correlation at Points P6, P8, and P10, where the landslides exhibited a linear evolution trend. The landslide displacements in Figs. 15(b), (d), and (f) can be further segmented into three major stages annually by visual interpretation, as indicated by the blue dashed rectangles. First, the landslide was in a stable state (Stage I), with very little precipitation from December 2016 to February 2017. It then began to deform along with small rainfall from March to May 2017. In particular, significant acceleration (Stage II) was observed, accompanied by heavy rainfall from June to August 2017, with a maximum monthly precipitation of 154 mm in June. A particular displacement evolution of the landslide was detected from August to December 2017, that is, the landslides exhibited a stable state during this period; however, the study area was still in the rainy season, with a monthly precipitation of approximately 111 mm. A notable acceleration of landslide displacement (Stage III) was also observed from September to December 2017. Furthermore, the displacement accelerated again (see the black dashed rectangles in Figs. 15(b), (d), and (f)) along with the emergence of strong precipitation in the summer of 2018. From the results of the correlation analysis between precipitation and water level changes in the Jinsha River as shown in Fig. 15(h), we can observe that there is a strong correlation between the water level changes in the Jinsha River and precipitation. That is, a sharp rise (see A marked in Fig. 15(h)) in the water level of the Jinsha River resulted from heavy rainfall and quick declines (see B marked in Fig. 15(h)) were observed with the decrease in rainfall. These findings suggest that the non-linear movement behaviour of the landslide at Points P5, P7 and P9 is likely caused by the water level fluctuations resulted from periodic heavy rainfall. Thus, we infer that the fluctuation of river water level is one of the major driving factors of landslide activity in the study area.

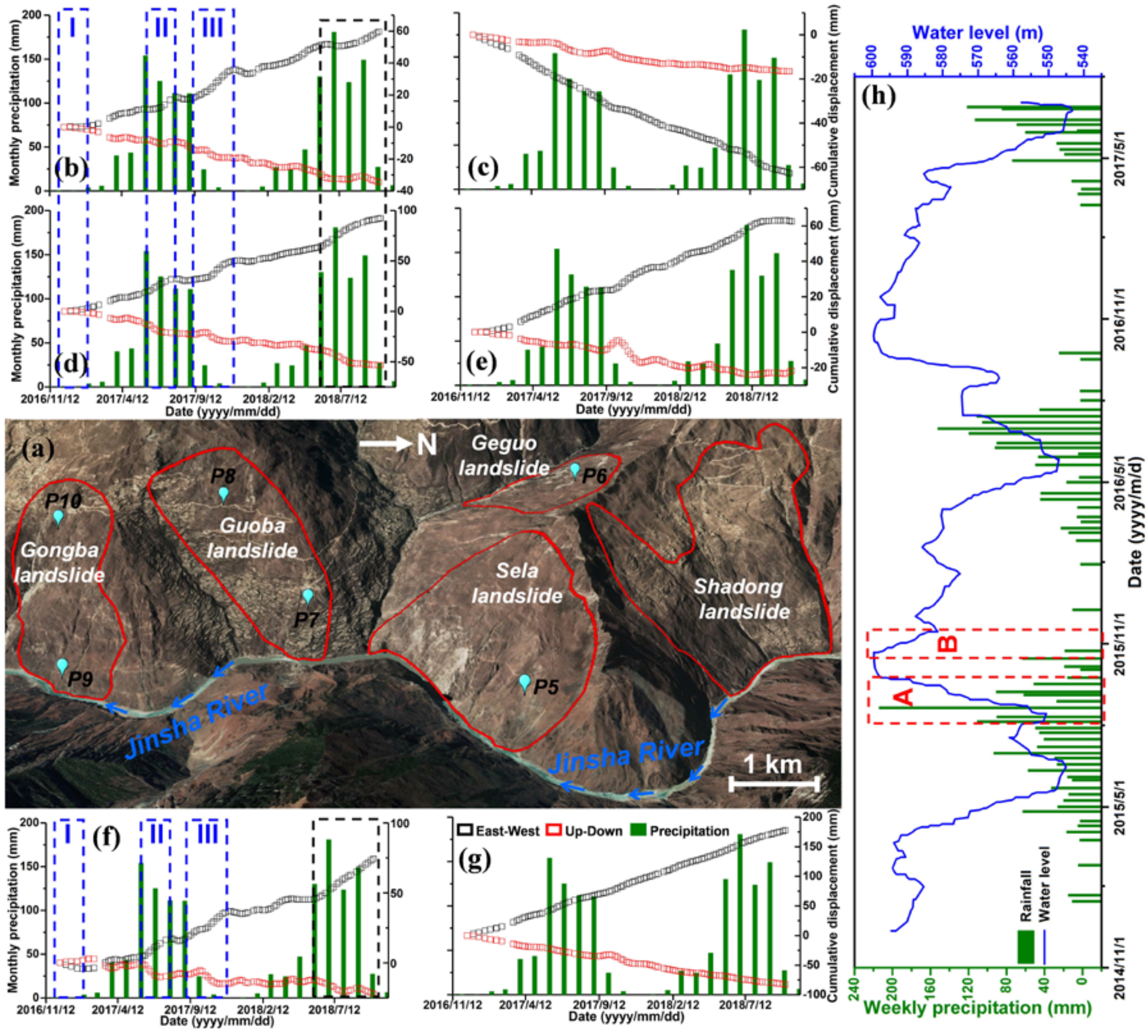

Fig. 15. Plots of 2D displacement time series of typical landslides versus monthly precipitation. (a) Optical image of the selected typical landslides, where the red lines are the boundary of the landslides, and the green circles indicate the locations of Points P5–P10; (b) P5; (c) P6; (d) P7; (e) P8; (f) P9; (g) P10; and (h) weekly precipitation in the Xiluodu reservoir area of the Jinsha River versus actual water level of the Jinsha River.

6 Conclusions

We presented a new approach for fusing C- and L-band SAR images to retrieve the 3D and long-term (nearly 12 years) displacement time series of landslides. Its performance was tested and validated by landslides over the Jinsha River in Gongjue County, China. The spatial distribution and spatiotemporal displacement patterns of landslides were retrieved using four SAR datasets of L-band ascending ALOS/PALSAR-1, C-band descending ENVISAT, and C-band ascending and descending Sentinel-1 acquired from January 2007 to November 2018. Moreover, the kinematic evolution and possible driving factors of landslide displacements were analyzed and discussed. Several conclusions can be drawn as follows:

First, 13 active landslides with diverse dimensions were detected and mapped with a total coverage of approximately 176 km^2, seven of which were larger than 2 km in either length or width. The two-dimensional displacement results revealed that the detected landslides had the different spatiotemporal displacement patterns and movement directions, which were strongly correlated with the geomorphological features of the slopes. In particular, the heterogeneous displacement pattern and movement direction of each block of the Shadong landslide were identified using 3D displacement rates and time series.

Second, nearly 12 years of displacement time series of the Shadong landslide were first retrieved by linking L-band ALOS/PALSAR-1 and C-band Sentinel-1 SAR images based on the Tikhonov regularization (TR) method. The experimental results indicated that the largest cumulative displacement of the Shadong landslide reached -1.33 m in the sliding direction from January 2007 to October 2018, and the kinematic evolution and creep behavior of the Shadong landslide were investigated using rock's unidimensional constitutive laws of Lomnitz 1956, 1957, Modified Lomnitz, and Aydan et al. 2003. The displacement observed by InSAR data fit well with that modelled by unidimensional constitutive laws. Therefore, we can conclude that the Shadong landslide may have been in the primary and secondary creep stages.

Third, the 2D nonlinear displacement time series were captured on the landslides near the Jinsha River, which corresponded directly to the river water level fluctuations that were caused by seasonal heavy rainfall. Consequently, the river water level fluctuations can be inferred as one of the major driving factors of landslide displacement.

Acknowledgments

This research was financially funded by the Natural Science Foundation of China (Grant Nos. 41731066, 41874005, 41790440), the Fundamental Research Funds for the Central University (Grant Nos. 300102269712 and 300102269303), and China Geological Survey Project (DD20190637 and DD20190647). This research was also supported by a Chinese Scholarship Council studentship awarded to Xiaojie Liu (Ref. 202006560031). Roberto Tomás was supported by the Spanish Ministry of Economy, Industry and Competitiveness (MINECO), the State Agency of Research (AEI) and European Funds for Regional Development (FEDER) under project TEMUSA (TEC2017-85244-C2-1-P). We thank the editors and eight anonymous reviewers for their constructive and insightful comments and suggestions.

References

Aydan, Ö., Ito, T., Özbay, U., Kwasniewski, M., Shariar, K., Okuno, T., Özgenoğlu, A., Malan, D.F., Okada, T., 2014. ISRM suggested methods for determining the creep characteristics of Rock. Rock Mech Rock Eng, 47, 275-290.

Ao, M., Zhang, L., Shi, X.G., Liao, M.S., Dong, J., 2019. Measurement of the three-dimensional surface deformation of the Jiaju landslide using a surface-parallel flow model. Remote Sensing Letters 10(8), 776-785.

Berardino, P., Fornaro, G., Lanari, R., Sansosti, E., 2002. A new algorithm for surface deformation monitoring based on small baseline differential SAR interferograms. IEEE Trans. Geosci. Remote Sens. 40(11), 2375–2383.

Burrows, K., Walters, R.J., Milledge, D., Spaans, K., Densmore, A., 2019. A new method for large-scale landslide classification from satellite radar. Remote Sensing 11, 237.

Cascini, L., Fornaro, G., Peduto, D., 2010. Advanced low- and full-resolution DInSAR map generation for slow-moving landslide analysis at different scales. Engineering Geology 112, 29-42.

Chen, J., Dai, F.C., Lv, T.Y., Cui, Z.J., 2013. Holocene landslide-dammed lake deposits in the Upper Jinsha River, SE Tibetan Plateau and their ages. Quaternary International 298, 107-113.

Chen, K.J., Avouac, J.P., Aati, S., Milliner, C., Zheng, F., Shi, C., 2020. Cascading and pulse-like ruptures during the 2019 Ridgecrest earthquakes in the Eastern California Shear Zone. Nature Communications 11, 1-8.

Chen, L.Q., Zhao, C.Y., Kang, Y., Chen, H.Y., Yang, C.S., Li, B., Liu, Y.Y., Xing, A.G., 2020. Pre-event deformation and failure mechanism analysis of the Pusa landslide, China with multi-sensor SAR imagery. Remote Sensing 12, 856.

Costantini, M., 1998. A novel phase unwrapping method based on network programming. IEEE Trans. Geosci. Remote Sens. 36 (3), 813–821.

Cruden, D.M., Varnes, D.J., 1996. Landslide types and process. In: Turner, A.K. & Schuster, R.L. (eds.) Landslides: investigation and mitigation (Special Report). National Research Council, Transportation and Research Board Special Report, Washington, DC, USA, 36–75.

Dong, J., Liao, M.S., Xu, Q., Zhang, L., Tang, M.G., Gong, J.Y., 2018. Detection and displacement characterization of landslides using multi-temporal satellite SAR interferometry: A case study of Danba County in the Dadu River Basin. Engineering Geology 240, 95-109.

Dai, K.R., Li, Z.H., Xu, Q., Bürgmann, R., Milledge, D.G., Tomás, R., Fan, X.M. et al., 2020. Entering the era of earth observation-based landslide warning systems: A novel and exciting framework. IEEE Geoscience and Remote Sensing Magazine 8(1), 136-153.

Eriksen, H., Lauknes, T., Larsen, Y., D. Corner, G., G. Bergh, S., Dehls, J., Kierulf, H.P., 2017. Visualizing and interpreting surface displacement patterns on unstable slopes using multi-geometry satellite SAR interferometry (2D InSAR). Remote Sensing of Environment 191, 297-312.

Frattini, P., B. Crosta, G., Rossini, M., Allievi, J., 2018. Activity and kinematic behaviour of deep-seated landslides from PS-InSAR displacement rate measurements. Landslides 15, 1053 - 1070.

Froude, M., Petley, D., 2018. Global fatal landslide occurrence from 2004 to 2016. Nat. Hazards Earth Syst. Sci. 18, 2161–2181.

Fukuzono, T., 1985. A new method for predicting the failure time of a slope failure. In: Proceeding of 4th International Conference and Field Workshop on Landslides, Tokyo (Japan), pp. 145-150.

Goldstein, R., Werner, C., 1998. Radar interferogram filtering for geophysical applications. Geophys. Res. Lett. 25 (21), 4035–4038.

Gourmelen, N., Kim, S.W., Shepherd, A., Park, J.W., Sundal, A.V., BjÖrnsson, H., Pálsson, F., 2011. Ice velocity determined using conventional and multiple-aperture InSAR. Earth Planet. Sci. Lett. 307 (1–2), 156–160.

Guo, C.B., R. Montgomery, D., Zhang, Y.S., Wang, K., Yang, Z.H., 2015. Quantitative assessment of landslide susceptibility along the Xianshuihe fault zone, Tibetan Plateau, China. Geomorphology 248, 93-110.

Handwerger, A.L., Fielding, E.J., Huang, M.H., Bennett, G.L., Liang, C.R., Schulz, W.H., 2019. Widespread Initiation, Reactivation, and Acceleration of Landslides in the Northern California Coast Ranges due to Extreme Rainfall. Journal Geophysical Research: Earth Surface 124(7), 1-16.

Hansen, P., O'Leary, D., 1993. The use of the L-curve in the regularization of discrete ill-posed problems. SIAM Journal on Scientific Computing 14(6), 1487–1503.

He, P., Wen, Y.M., Xu, C.J., Chen, Y.G., 2019. Complete three-dimensional near-field surface displacements from imaging geodesy techniques applied to the 2016 Kumamoto earthquake. Remote Sensing of Environment 232, 111321.

Herrera, G., Gutiérrez, F., García-Davalillo, J.C., Guerrero, J., Notti, D., Galve, J.P., Fernández-Merodo, J.A., Cooksley, G., 2013. Multi-sensor advanced DInSAR monitoring of very slow landslides: The Tena Valley case study (Central Spanish Pyrenees). Remote Sensing of Environment 128, 31-43.

Hu, J., Li, Z.W., Ding, X.L., Zhu, J.J., Zhang, L., Sun, Q., 2014a. Resolving three-dimensional surface displacements from InSAR measurements. Earth-Science Reviews 133, 1-17.

Hu, J., Li, Z.W., Li, J., Zhang, L., Ding, X.L., Zhu, J.J., Sun, Q., 2014b. 3-D movement mapping of the alpine glacier in Qinghai-Tibetan Plateau by integrating D-InSAR, MAI and Offset-Tracking: Case study of the Dongkemadi Glacier. Global and Planetary Change 118, 62-68.

Hu, X., Bürgmann, R., Lu, Z., Handwerger, A. L., Wang, T., Miao, R., 2019. Mobility, thickness, and hydraulic diffusivity of the slow-moving Monroe landslide in California revealed by L-band satellite radar interferometry. Journal of Geophysical Research: Solid Earth 124, 1-15.

Hu, X., Lu, Z., Pierson, T.C., Kramer, R., George, D.L., 2018. Combining InSAR and GPS to determine transient movement and thickness of a seasonally active low-gradient translational landslide. Geophysical Research Letters 45, 1-10.

Hu, X., Wang, T., Pierson, T.C., Lu, Z., Kim, J.W., Cecere, T.H., 2016. Detecting seasonal landslide movement within the Cascade landslide complex (Washington) using time-series SAR imagery. Remote Sensing of Environment 187, 49-61.

Intrieri, E., Carlà, T., Gigli, G., 2019. Forecasting the time of failure of landslides at slope-scale: A literature review. Earth-Science Reviews 193, 333-349.

Intrieri, E., Frodella, W., Raspini, F., Bardi, F., Tofani, V., 2020. Using satellite interferometry to infer landslide sliding surface depth and geometry. Remote Sensing 12, 1462.

Jo, M.J., Jung, H.S., Won, J.S. Measurement of precise three-dimensional volcanic deformations via TerraSAR-X synthetic aperture radar interferometry. Remote Sensing of Environment 192. 228-237.

Kang, Y., Zhao, C.Y., Zhang, Q., Lu, Z., Li, B., 2017. Application of InSAR Techniques to an Analysis of the Guanling Landslide. Remote Sensing 9, 1046.

Lacroix, P., Handwerger, A.L., Bièvre, G., 2020. Life and death of slow-moving landslides. Nature Reviews Earth & Environment 1, 404-419.

Li, M.H., Zhang, L., Shi, X.G., Liao, M.S., Yang, M.S., 2019. Monitoring active motion of the Guobu landslide near the Laxiwa Hydropower Station in China by time-series point-like targets offset tracking. Remote Sensing of Environment 221, 80-93.

Li, X., Guo, C.B., Yang, Z.H., Liao, W., Wu, R.A., Jin, J.J., He, Y.X., 2021. Development characteristics and formation mechanism of the Xiongba giant ancient landslide in the Jinshajiang tectonic zone. Geoscience 35(1), 47-55. (In Chinese)

Li, Y., Fan, X.Y., Cheng, G.W., 2006. Landslide and rockfall distribution by reservoir of stepped hydropower station in the Jinsha River. Wuhan University Journal of Natural Science 4, 801-805.

Lin, Q.G., Wang, Y., 2018. Spatial and temporal analysis of a fatal landslide inventory in China from 1950 to 2016. Landslides 15, 2357-2372.

Lu, Y.F., 2015. Deformation and failure mechanism of slope in three dimensions. Journal of Rock Mechanics and Geotechnical Engineering 7, 109-119.

Lu, H.Y., Li, W.L., Xu, Q., Dong, X.J., Dai, C., Wang, A., 2019. Early detection of landslides in the upstream and downstream areas of the Baige landslide, the Jinsha River based on optical remote sensing and InSAR technologies. Geomatics and Information Science of Wuhan University 44, 1342-1354.

Lyons, S., Sandwell, D., 2003. Fault creep along the southern San Andreas from interferometric synthetic aperture radar, permanent scatterers, and stacking. J. Geophys. Res. Solid Earth 108.

Ma, D.T., Tu, J.J., Cui, P., Lu, R.R., 2004. Approach to Mountain Hazards in Tibet, China. Journal of Mountain Science 2, 143-154.

Marquardt, D., 1963. An algorithm for least square estimation on non-linear parameters. SIAM J. APPL. MATH. 11, 431-441.

Pepe, A., Bonano, M., Zhao, Q., Yang, T.L., Wang, H.M., 2016a. The use of C-/X-band time-gapped SAR data and geotechnical models for the study of Shanghai’s ocean-reclaimed lands through the SBAS-DInSAR technique. Remote Sensing 8, 911.

Pepe, A., Solaro, G., Calo, F., Dema, C., 2016b. A Minimum Acceleration Approach for the Retrieval of Multiplatform InSAR Deformation Time Series. IEEE Journal of Selected Topics in Applied Earth Observations and Remote Sensing 9(8), 3883-3898.

Piciullo, L., Calvello, M., Cepeda, J.M., 2018. Territorial early warning systems for rainfall-induced landslides. Earth-Science Reviews 179, 228-247.

Raucoules, D., de Michele, M., MaletC, J.P., Ulrich, P., 2013. Time-variable 3D ground displacements from high-resolution synthetic aperture radar (SAR). Application to La Valette landslide (South French Alps). Remote Sensing of Environment 139, 198-204.

Samsonov, S., 2019. Three-dimensional deformation time series of glacier motion from multiple-aperture DInSAR observation. Journal of Geodesy 93, 2651-2660.

Samsonov, S., d’Oreye, N., Smets, B, 2013. Ground deformation associated with post-mining activity at the French–German border revealed by novel InSAR time series method. International Journal of Applied Earth Observation and Geoinformation 23, 142-154.

Samsonov, S., d'Oreye, N., González, J., Tiampo, K., Ertolahti, L., Clague, J., 2014. Rapidly accelerating subsidence in the Greater Vancouver region from two decades of ERS-ENVISAT-RADARSAT-2 DInSAR measurements. Remote Sensing of Environment 143, 180-191.

Samsonov, S., Tiampo, K., Rundle, J., Li, Z.H., 2007. Application of DInSAR-GPS optimization for derivation of fine-scale surface motion maps of southern California. IEEE Trans. Geosci. Remote Sens. 45 (2), 512–521.

Satio, M., 1969. Forecasting time of slope failure by tertiary creep. In Proceeding of 7th International Conference on Soil Mechanics and Foundations Engineering, Montreal (Canada), pp. 667-683.

Schaefer, L.N., Traglia, F.D., Chaussard, E., Lu, Z., Nolesini, T., Casagli, N., 2019. Monitoring volcano slope instability with Synthetic Aperture Radar: A review and new data from Pacaya (Guatemala) and Stromboli (Italy) volcanoes. Earth-Science Reviews 192, 236-257.

Shi, X.G., Yang, C., Zhang, L., Jiang, H.J., Liao, M.S., Zhang, L., Liu, X.G., 2019. Mapping and characterizing displacements of active loess slopes along the upstream Yellow River with multi-temporal InSAR datasets. Science of the Total Environment 674, 200-210.

Shi, X.G., Zhang, L., Balz, T., Liao, M.S., 2015. Landslide deformation monitoring using point-like target offset tracking with multi-mode high-resolution TerraSAR-X data. ISPRS Journal of Photogrammetry and Remote Sensing 105, 128-140.

Shi, X.G., Zhang, L., Zhang, Y.L., Zhang, L., Liao, M.S., 2020. Detection and characterization of active slope deformations with Sentinel-1 InSAR analyses in the southwest area of Shanxi, China. Remote Sensing 12, 392.

Shi, X.G., Zhang, L., Zhou, C., Li, M.H., Liao, M.S., 2018. Retrieval of time series three-dimensional landslide surface displacements from multi-angular SAR observations. Landslides 15, 1015-1027.

Sun, Q., Hu, J., Zhang, L., Ding, X.L., 2016. Towards Slow-Moving Landslide Monitoring by Integrating Multi-Sensor InSAR Time Series Datasets: The Zhouqu Case Study, China. Remote Sensing 8, 908.

Tikhonov, A., 1963. Solution of incorrectly formulated problems and the regularization method. Soviet Math. Dokl. 4, 1035–1038.

Tong, X.H., Liu, S., Li, R.X., Xie, H., Liu, S.J., Qiao, G., Feng, T.T., Tian, Y.X., Ye, Z., 2018. Multi-track extraction of two-dimensional surface velocity by the combined use of differential and multiple-aperture InSAR in the Amery Ice Shelf, East Antarctica. Remote Sensing of Environment 204, 122-137.

Varnes, D., 1996. Landslide types and processes. Landslides-invesitgation and mitigation 247, 36-75.

Wang, S.J., Li, G.H., Zhang, Q., Lan, C.L, 2000. Engineering geological study of the active tectonic region for hydropower development on the Jinsha River, upstream of the Yangtze River. Acta Geologica Sinica 74(2), 353-361.

Wang, T., Jonsson, S., 2015. Improved SAR amplitude image offset measurements for deriving three-dimensional coseismic displacements. IEEE Journal of Selected Topics in Applied Earth Observations and Remote Sensing 8, 3271–3278.

Wasowski, J., Bovenga, F., 2014. Investigation landslides and unstable slopes with satellite multi temporal interferometry: Current issues and future perspectives. Engineering Geology 174, 103-138.

Wasowski, J., Pisano, L., 2020. Long-term InSAR, borehole inclinometer, and rainfall records provide insight into the mechanism and activity patterns of an extremely slow urbanized landslide. Landslides 17, 445–457.

Wright, T.J., Parsons, B.E., Lu, Z., 2004. Toward mapping surface deformation in three dimensions using InSAR. Geophysical Research Letters 31, L01607.

Wu, S.B., Yang, Z.F., Ding, X.L., Zhang, B.C., Zhang, L., Lu, Z., 2020. Two decades of settlement of Hong Kong International Airport measured with multi-temporal InSAR. Remote Sensing of Environment 248, 111976.

Yin, Y.P., Wang, F.W., Sun, P., 2009. Landslide hazards triggered by the 2008 Wenchuan earthquake, Sichuan, China. Landslides 6, 139-151.

Zhao, C.Y., Kang, Y., Zhang, Q., Lu, Z., Li, B., 2018. Landslide identification and monitoring along the Jinsha River catchment (Wudongde reservoir area), China, using the InSAR method. Remote Sensing 10, 993.

List of Figure Captions

Fig. 1. Location of the study area and coverage of the synthetic aperture radar (SAR) images, with SRTM DEM as the base map. The white and black rectangles represent the study area and the coverage of the SAR images, respectively, and the red dots are the earthquakes that occurred in the study area and vicinity during the period of 1954 to 2019. The red lines are the faults modified from Li et al., 2021, where F1: Jinsha River East Fault; F2: Jinsha River Main Fault; F3: Xiongsong-Suwalong Fault; and F4: Batang Fault.

Fig. 2. (a) Geological setting of the study area, with the scale of 1: 250000. The name of the labeled landslides (i.e., No.1 ~ No.13) is listed in Table 2, and the red lines indicate the faults. (b) Shaded relief map of the Shadong

landslide, labeled as No.2 in (a). The polygons with different colors represent five blocks (B1-B5) of the landslide. (c) Geological cross section along the Profile I-I' marked in (b), adapted from Li et al., 2021.

Fig. 3. Spatial-temporal baseline combinations of all interferograms used in this study. (a) ALOS/PALSAR-1 dataset for Path 484; (b) ENVISAT dataset for Path 190; (c) ascending Sentinel-1 dataset for Path 99; and (d) descending Sentinel-1 dataset for Path 33.

Fig. 4. Flowchart of 3D and long-term displacement time series estimation and mechanism analysis of landslide.

Fig. 5. Line-of-sight (LOS) displacement rate maps for the study area derived from (a) ascending ALOS/PALSAR-1 images between January 2007 and March 2011; (b) descending ENVISAT images between February 2007 and October 2010; (c) ascending Sentinel-1 images between August 2016 and October 2018; and (d) descending Sentinel-1 images between December 2016 and November 2018. The labels indicate the name of the detected landslides listed in Table 2, and the white solid polygons indicate the boundaries of the landslides.

Fig. 6. Location and extent of the main detected active landslides on the perspective remote sensing image. The points indicate the location of the main villages placed in the study area.

Fig. 7. Two-dimensional displacement rate maps of the detected landslides from December 2016 to October 2018 calculated with ascending and descending Sentinel-1 images. The white solid polygons indicate the boundaries of the landslides. (a) Horizontal east-west displacement rate map; and (b) vertical displacement rate map.

Fig. 8. Remote sensing image and 3D displacement rate maps from December 2016 to October 2018 of the Shadong landslide. The boundary of the landslide movement is marked using the red solid lines, and the black dotted polygons (i.e., R1 and R2) in (b) indicate the two secondary sliding regions. (a) Remote sensing image acquired in March 2015, where different colors represent five blocks of the landslide; (b) north-south displacement rate map; (c) east-west displacement rate map, from which Points P1–P4 are analyzed in the text to show displacement time series; and (d) vertical displacement rate map, where two black lines indicate the locations of Profiles AA' and BB'.

Fig. 9. Displacement rates along the three components and elevation along the Profiles AA' and BB' labeled in Fig. 8(d). (a) Profile AA'; and (b) Profile BB', where B1, B2 and B3–B4 indicate block 1, block 2 and blocks 3-4 of the Shadong landslide labeled in Fig. 8(a), respectively.

Fig. 10. (a) The horizontal movement vector of the Shadong landslide; and (b) the enlarged horizontal movement vector over Region R1 marked in Fig. 8(b). The base map is the UAV image acquired on 13 June 2020, with a spatial resolution of 0.3 m.

Fig. 11. Three-dimensional displacement rate maps of Region R1 marked in Fig. 8(b). (a) UAV image acquired on 13 June 2020; (b) north-south displacement rate; (c) east-west displacement rate; and (d) vertical displacement rate.

Fig. 12. The displacement time series along the three main components for Points P1–P4 (marked in Fig. 8(c)) of the Shadong landslide from December 2016 to October 2018. (a) P1; (b) P2; (c) P3; and (d) P4.

Fig. 13. One-dimensional long-term displacement time series in the sliding direction of the Shadong landslide for Points P1–P4 calculated by fusing L-band ALOS/PALSAR-1 and C-band Sentinel-1 SAR measurements from January 2007 to October 2018. (a) P1; (b) P2; (c) P3; and (d) P4.

Fig. 14. Kinematic evolution and creep behavior of the Shadong landslide from January 2007 to October 2018. (a) Standard three-stage creep rupture curve of the slope (modified after Fukuzono, 1985; Intrieri et al., 2019; and Saito, 1969); (b) displacement time series (in the sliding direction) of the Shadong landslide for Point P1 derived from InSAR observations (black squares) versus that derived by modeling of rock's unidimensional constitutive laws (blue line); (c) displacement time series of Point P3 derived by InSAR observations (black squares) versus that derived by modelling (red and blue lines); (d) Residuals of Point P1, calculated by subtracting the modeled values (using Modified Lomnitz law) from the observed values; (e) Residuals of Point P3, calculated by subtracting the modeled values (using Lomnitz 1956, 1957) from the observed values. The locations of Points P1 and P3 are marked in Fig. 8(c).

Fig. 15. Plots of 2D displacement time series of typical landslides versus monthly precipitation. (a) Optical image of the selected typical landslides, where the red lines are the boundary of the landslides, and the green

circles indicate the locations of Points P5–P10; (b) P5; (c) P6; (d) P7; (e) P8; (f) P9; (g) P10; and (h) weekly precipitation in the Xiluodu reservoir area of the Jinsha River versus actual water level of the Jinsha River.